A&A, 707, A324 (2026)
https://doi.org/10.1051/0004-6361/202557860

Astronomy & Astrophysics

Physical properties of long-rising type II supernovae

Bayesian analytic modeling and spectrophotometric correlations

S. P. Cosentino[1,2,⋆], C. Inserra[3], and M. L. Pumo[1,2,4]

[1] Dipartimento di Fisica e Astronomia "Ettore Majorana", Università degli Studi di Catania, Via Santa Sofia 64, 95123 Catania, Italy
[2] INAF – Osservatorio Astrofisico di Catania, Via Santa Sofia 78, 95123 Catania, Italy
[3] Cardiff Hub for Astrophysics Research and Technology, School of Physics & Astronomy, Cardiff University, Queens Buildings, The Parade, Cardiff CF24 3AA, UK
[4] INFN – Laboratori Nazionali del Sud, Via S. Sofia 62, 95125 Catania, Italy

Received 27 October 2025 / Accepted 7 February 2026

ABSTRACT

Context. The supernova (SN) 1987A, with its long-rising (≳40 days) light curve, defines a rare subclass of type II SNe known as 1987A-like events. Representing only ∼1–3% of all core-collapse SNe and often found in low-metallicity environments, their large diversity suggests a wide range of progenitor and explosion properties.
Aims. Our aim with this study is to improve the understanding of 1987A-like SNe by characterizing their explosion parameters, including kinetic energy, ejected mass, progenitor radius at the explosion, and synthesized ^{56}Ni mass. Additionally, we seek to identify systematic trends in both the physical properties and the observed spectrophotometric features of these peculiar events.
Methods. A new Bayesian parameter estimation method based on our ^{56}Ni-dependent analytical model for hydrogen-rich SNe is applied to derive explosion parameters from the light curves and expansion velocities of one of the largest and most comprehensive 1987A-like SN samples to date. These data are measured through a consistent analysis of observations available in the literature.
Results. The analysis reveals a heterogeneous population that nevertheless clusters into two main groups: (i) lower-energy explosions with modest ^{56}Ni yields (∼0.07 $M_\odot$), similar to SN 1987A, and (ii) more energetic events (up to ∼5 foe) with larger nickel production and, in some cases, unusually extended progenitors. We confirm a robust correlation between ^{56}Ni mass, peak luminosity, and explosion energy, as well as between ejecta mass and the recombination timescale. An anticorrelation between Ba II line strength and photospheric velocity indicates that stronger Ba II absorptions in 1987A-like SNe arise from more compact, slowly expanding ejecta.
Conclusions. Our findings indicate that 87A-like SNe populate a continuous distribution of explosion energies and progenitor radii. The study underscores the need to extend analytical frameworks to include additional power sources that will enable scalable and accurate modeling of the growing number of peculiar transients that will be discovered by current and upcoming surveys (e.g., ZTF and LSST).

Key words. methods: analytical – methods: data analysis – methods: statistical – supernovae: general – supernovae: individual: 1987A-like SNe

1. Introduction

The explosion of Supernova (SN) 1987A, located only ≈50 kpc from Earth in the direction of the Large Magellanic Cloud (LMC), was an extraordinary event that significantly advanced our understanding of core-collapse (CC) SN events and progenitor stars (e.g., Burrows 1990; Woosley et al. 2002). The unusual shape of its long-rising (≈80 days) light curve (LC) is consistent with the explosion of a compact blue supergiant (BSG) progenitor (Arnett et al. 1989; Kleiser et al. 2011; Orlando et al. 2015). The slow brightness rise and the LC secondary peak, characteristic features of SN 1987A, make it the prototype of a peculiar subclass of H-rich SN events, referred to as long-rising (typically ≳40 days) type II SNe (SNe II), or simply 1987A-like events (e.g., Turatto et al. 2007; Pastorello et al. 2012; Taddia et al. 2016; Pumo et al. 2023, hereafter Paper I).

Notably, 1987A-like SNe are intrinsically rare events, with observational estimates suggesting they account for only ≈1−3% of all CC-SNe (Smartt 2009; Pastorello et al. 2012; Taddia et al. 2016; Sit et al. 2023, who recently reported a volumetric rate of about 1.37×10^{-6} Mpc^{-3} yr^{-1}). Their rarity reflects the limited evolutionary pathways through which a massive star (with a zero age main sequence mass of $M_{\rm ZAMS} \gtrsim 8-10\,M_\odot$; e.g., Pumo et al. 2009) can become a BSG prior to its explosion as a CC-SN.

Although the sample of long-rising SNe II is statistically limited, their bolometric LCs exhibit significant variation in rise time ($t_{\rm M}$) and the maximum luminosity ($L_{\rm M}$) of the secondary peak (Paper I). This peak, taking place during the hydrogen recombination phase, is commonly interpreted as the result of the interplay between the cooling driven by the SN expansion rate and heating from the radioactive decay of isotopes, primarily ^{56}Ni, synthesized during the explosion (see, e.g., Popov 1993; Utrobin & Chugai 2011; Pumo & Zampieri 2011; Pumo & Cosentino 2025, hereafter Paper II).

Modeling the LC peak and analysing its main features allow us to infer key physical properties of the ejected material (hereafter the ejecta), including the explosion energy (E), progenitor radius (R_0), total ejecta mass ($M_{\rm ej}$), and the mass of radioactive ^{56}Ni ($M_{\rm Ni}$). These quantities, in turn, provide crucial insights into the progenitor's nature and the explosion mechanism (e.g., Arnett 1996; Kasen & Woosley 2009; Pumo & Zampieri 2013; Fang et al. 2024).

⋆ Corresponding author: stefano.cosentino@dfa.unict.it

Previous studies about long-rising SNe have identified several clones of SN 1987A (e.g., SN 2009E, SN 2009mw, and SN 2018hna; see also Pastorello et al. 2012; Takáts et al. 2016; Singh et al. 2019), which are characterized by peak luminosities below 2×10^{42} erg s^{-1} and rise times of approximately 70–90 days. These events are generally interpreted as CC-explosions with energies in the range of ∼0.5−5 foe (1 foe ≡ 10^{51} erg), originating from relatively compact ($R_0 \sim 30-100\,R_\odot$) and massive ($M_{ej} \sim 15-20\,M_\odot$) progenitors (see Paper I, and references therein). The ^{56}Ni masses powering their tail luminosities typically range from $M_{Ni} \sim 0.05-0.1\,M_\odot$, higher than those of standard type II-plateau (IIP) SNe (see, e.g., Pastorello et al. 2012; Müller et al. 2017; Rodríguez et al. 2021).

There is also evidence that similar long-rising LCs can originate from non-BSG progenitors ($R_0 \gtrsim 300\,R_\odot$) capable of synthesizing substantial amounts of ^{56}Ni ($M_{Ni} \gtrsim 0.1\,M_\odot$). Examples include SN 2004ek and SN 2004em, which have been described by Taddia et al. (2016) as intermediate events bridging the gap between the clones of SN 1987A and typical SNe IIP. The discovery of brighter 1987A-like objects, including PTF12kso and PTF12gcx (Taddia et al. 2016), seems to indicate the existence of Ni-rich ($\gtrsim$0.1−0.2 $M_\odot$) and high-energy ($\gtrsim$5−10 foe) events forming a luminous tail of 1987A-like events, which could be characterized by a non-conventional explosion (Paper I). Among these events, OGLE-2014-SN-073 (hereafter OGLE-14) stands out as the brightest long-rising SN (Terreran et al. 2017). With a redshift of $z \simeq 0.12$, it is also the most distant of 1987A-like SNe, second only to the gravitationally lensed SN Refsdal ($z \simeq 1.49$, see Kelly et al. 2016). OGLE-14 is characterized by a peak bolometric luminosity of approximately 10^{43} erg s^{-1} and a rise time of about 100 days. Its extraordinary LC challenges explanation within the framework of the conventional neutrino-driven CC paradigm and has been linked to pair-instability scenarios (Terreran et al. 2017). An alternative explanation for this exceptional event involves the presence of a prompt injection of energy from a compact internal engine (e.g., magnetar) following the explosion. Such a mechanism has also been proposed for more recent and nearby analogous events, including SN 2020faa (Yang et al. 2021; Salmaso et al. 2023) and SN 2021aatd (Szalai et al. 2024). The influence of additional energy sources, such as ^{56}Ni–^{56}Co decay, magnetar spin-down, or accretion onto a compact object, can extend the long-rising phase and alter the late-time LC (e.g., Kasen & Bildsten 2010; Inserra et al. 2013; Dexter & Kasen 2013; Khatami & Kasen 2019; Matsumoto et al. 2025, and further comments in Paper II). These additional energy sources can give rise to long-lived events such as SN DES16C3cje (Gutiérrez et al. 2020), which exhibited a rise time of approximately 140 days, followed by a decline consistent with fall-back accretion power after 300 days.

Despite their significance, fundamental questions persist regarding 1987A-like SNe, primarily due to the absence of sufficiently accurate and efficient methods for characterizing their physical properties (Paper I; Paper II). Moreover, the available information about the physical properties of the studied sample remains too limited and uncertain to draw definitive conclusions (Paper I). Form 2018 June to 2021 December, the sample of 1987A-like SNe has nearly doubled thanks to the systematic study by Sit et al. (2023) as part of the Census of the Local Universe (CLU; Cook et al. 2019) experiment conducted with the Zwicky Transient Facility (ZTF; Bellm et al. 2018; Graham et al. 2019) on galaxies at less than 200 Mpc ($z \lesssim 0.05$). This study presented the LCs and spectra of 13 additional long-rising SNe. However, a complete physical characterization of their progenitors and explosion mechanisms is still missing.

With the aim of improving our understanding of long-rising type II SN explosions, we present a new Bayesian parameter estimation method based on the LC analytical model developed in Paper II. This approach enables us to infer the physical properties of SN progenitors at the explosion, including E, M_{ej}, R_0, and M_{Ni}. In this paper, after presenting this method and validating its accuracy (Sect. 2), we apply it to one of the largest and most comprehensive samples of well-observed 1987A-like objects (Sect. 3). Finally, we conduct a global study inside 1987A-like class of their explosion parameters in relation to the measured spectrophotometric features (Sect. 4). The key results are outlined in Section 5, and we highlight their significance in interpreting the nature of these peculiar events.

2. "Fast" SN modeling procedures

The physical characterization of long-rising SNe II can be approached through various modeling methods, each balancing computational complexity and accuracy. The most detailed analyses employ full-numerical hydrodynamic simulations, which incorporate a wide range of physical phenomena, including relativistic hydrodynamics and nuclear heating processes (e.g., Pumo & Zampieri 2011; Bersten et al. 2011). Although the numerical hydrodynamic modeling (HM) is highly accurate, it is computationally expensive and less practical for statistical studies of a heterogeneous sample of peculiar events, such as 1987A-like SNe. A more rapid but less precise alternative is the use of scaling relations, which connect the SN physical parameters to observables through simple proportionality relations. However, the accuracy of this method diminishes when the observed SNe differ significantly from the reference event (e.g., Paper I, and references therein). Intermediate approaches, such as analytical or semi-analytical models, stand out as the most practical solution, as they significantly reduce the complexity of full numerical simulations, minimizing computational time (thus being "faster") while still capturing the main physical processes involved in the SN post-explosive evolution (see, e.g., Paper II, and references therein).

Among the most well-known and widely used analytic models for H-rich SNe, including 1987A-like events, are those developed by Arnett (1980, 1996) and Arnett et al. (1989), which describe the behavior of the bolometric LC dominated by the diffusion of photons through the expanding SN ejecta. These models are particularly effective during the early post-explosive phases, when hydrogen recombination does not yet significantly influence the cooling emission. For the later stages, when hydrogen recombination becomes important, the standard analytical framework is provided by Popov (1993). Furthermore, this model excludes the presence of additional heating effects, such as those from radioactive decay (e.g., ^{56}Ni–^{56}Co elements), ejecta interactions with the circumstellar medium (CSM), or energy injection from a central compact object. Subsequent analytical approaches have included these additional energy sources retaining the diffusive approximation of Arnett's models (see, e.g., Chatzopoulos et al. 2012; Inserra et al. 2013; Nicholl et al. 2017; Villar et al. 2017). More recently, similar mechanisms have been analytically incorporated into models for H-rich SNe, allowing for the evaluation of heating source effects on the SN LC even during phases where hydrogen recombination dominates (e.g., Dexter & Kasen 2013; Matsumoto et al. 2025, and Paper II). Specifically, Paper II's model is the first analytical description to account for different ^{56}Ni distributions and their

effect on radioactive heating at the recombination front. These features make it a valuable description for developing new modeling procedures aimed at accurately and efficiently determining the explosion and progenitor parameters of 1987A-like events. In the following, we present our implementation of this framework (Sect. 2.1) and assess its performance by comparing results for a set of well-studied 1987A-like SNe against HM benchmarks (Sect. 2.2).

2.1. Supernova bayesian analytic modeling – SuperBAM

"Supernova Bayesian Analytic Modeling" (SuperBAM) is a novel modeling approach based on Bayesian statistics and the analytical model presented in Paper II. It characterizes key physical properties of H-rich SNe, including $M_{\rm Ni}$, E, $M_{\rm ej}$, and R_0, through the analysis of the bolometric LC shape during the recombination phase (e.g., Pumo & Zampieri 2011). To achieve this, SuperBAM follows a three-phase process:

1. Prior information – SuperBAM extracts key spectrophotometric features from SN observations to construct prior probability distributions using appropriate scaling equations.
2. Likelihood definition – A likelihood function for the modeling parameters is defined by comparing analytical model predictions with observed data.
3. Posterior exploration – Priors and likelihoods are combined to obtain the posterior distribution, which is then analysed to determine the best-fit SN parameters.

These steps are detailed in the following subsections.

2.1.1. Prior information

SuperBAM employs physically motivated priors based on empirical scaling relations that link observable quantities, such as LC morphology and photospheric velocity, to the SN explosion parameters. This approach naturally narrows the parameter space without enforcing arbitrary boundaries, thus improving convergence efficiency and reducing the risk of bias near the edges of the physically plausible domain (see, e.g., Silva-Farfán et al. 2024). In contrast to a blind, uniform search over the full multidimensional parameter space (E, $M_{\rm ej}$, R_0, $M_{\rm Ni}$), this method enables a faster and more robust determination of the most probable physical configuration for each SN.

To automatically identify the LC characteristics necessary for defining prior probability, SuperBAM employs a gaussian process regression[1] (GPR), which permits interpolation of the LC, facilitating both its analysis and the computation of its derivative (see, e.g., Fig. 13 in Paper II). To select the best combination of mean function and kernel[2] for reproducing light and velocity curves, we tested several configurations using SN 1987A data. In these tests, the curves were artificially down-sampled by randomly removing individual points or entire observing periods of up to 30 days. By comparing the reconstructed values from the GPR against the original data via the mean square deviation, we identified the Matérn 3/2 kernel with a constant mean function as the most effective regression method for this type of data. The Matérn 3/2 kernel models functions with continuous derivatives up to the second order (e.g., Roberts et al. 2013), enabling the reconstruction of smooth profiles even when significant variations in the derivative or changes in concavity are present, as commonly observed in the 1987A-like LCs (see Fig. 1). Since the LC behavior of SN 1987A is representative of the class, the same GPR setup is adopted for all other 1987A-like events.

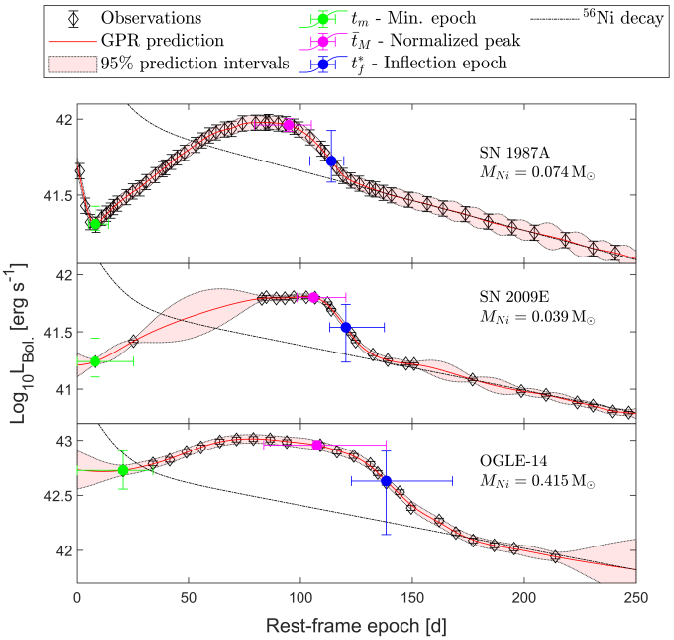

Fig. 1. Application of GPR to the bolometric LCs of SN 1987A, SN 2009E, and OGLE-14 taken from the literature (see Ref. in Sect. 2.2) to identify the main LC features. The adopted GPR employs a constant mean function combined with a Matérn 3/2 kernel. For each SN LC, the key epochs $t_{\rm m}$, $\bar{t}_{\rm M}$, and $t_{\rm f}^*$ are highlighted. The dashed line shows the luminosity contribution $L_{\rm Ni}$ due to ^{56}Ni–^{56}Co radioactive decay with $M_{\rm Ni}$ value reported within the panel of each SN.

Once the entire LC is reconstructed through GPR, three characteristic epochs ($t_{\rm m}$, $\bar{t}_{\rm M}$, and $t_{\rm f}^*$) are identified to estimate prior constrains. The first one is $t_{\rm m}$, defined as the epoch of minimum bolometric luminosity after the SN breakout but preceding the maximum of the secondary peak, and it is generally associated with the beginning of the hydrogen recombination (i.e., $t_{\rm i}$; see also Paper I). The other two epochs, $\bar{t}_{\rm M}$ and $t_{\rm f}^*$, were already introduced in Paper II and are defined in terms of the bolometric magnitude (i.e., $M_{\rm bol} \equiv -2.5\log_{10} L_{\rm bol} + 88.7$). Specifically, $\bar{t}_{\rm M}$ corresponds to the normalized peak's maximum where the derivative of $M_{\rm bol}$ equals to $-2.5\log_{10} e/(111\,{\rm day})$, i.e., the slope of the ^{56}Co decay tail ($\tau_{^{56}{\rm Co}} \simeq 111$ day; cf. Eq. (22) in Paper II), while $t_{\rm f}^*$ is the epoch of maximum derivative, corresponding to the inflection point of $M_{\rm bol}$ that marks the end of the recombination phase. The uncertainties on these epochs depend both on the GPR reconstruction, strongly linked to the number of observations available in the corresponding LC phase, and on the LC morphology (see Sect. 2.2 for further details). Moreover, the $t_{\rm f}^*$ positive error is constrained by the first epoch after the inflection where $\dot{M}_{\rm bol} \simeq -2.5\log_{10} e/(111\,{\rm d})$, which defines the beginning of the radioactive tail.

Considering all observations taken after the upper limit of $t_{\rm f}^*$, the ^{56}Ni mass can be directly estimated by fitting these LC points with the ^{56}Ni–^{56}Co radioactive luminosity, $L_{\rm Ni}(t) = M_{\rm Ni}\times$

[1] The GPR is a nonparametric supervised learning method used to solve regression problems. The GPR assumes that the N observed variables $L = (L_1, \ldots, L_{\rm N})^T$ are randomly drawn from a multivariate Gaussian distribution $f(m, K)$, where $m = (\mu_1, \ldots \mu_{\rm N})^T$ is the mean vector for each variable and K is their covariance matrix (NxN), also called kernel (Roberts et al. 2013). A GPR is hence specified by its mean function and kernel (see, e.g., Inserra et al. 2018).

[2] For a complete list of explored kernels, see also GPR MATLAB Documentation.

$\epsilon(t)$, where $\epsilon(t)$ is the specific energy release rate (erg g^{-1} s^{-1}) from the ^{56}Ni → ^{56}Co → ^{56}Fe decay chain (see Eq. (22) in Paper II). In 1987A-like SNe, the trapping of γ-rays from ^{56}Ni–^{56}Co decay remains efficient even beyond 300−400 days (see Paper II, and references therein). Since $t_{\rm f}^{*} \gg \tau_{^{56}\rm Ni} \simeq 8.8$ d, the ^{56}Ni–^{56}Co radioactive luminosity for $t > t_{\rm f}^{*}$ can be expressed as:

$$L_{\rm Ni}(t) \simeq M_{\rm Ni} \times \frac{\epsilon_{^{56}\rm Co}\, \tau_{^{56}\rm Ni}}{\tau_{^{56}\rm Co} - \tau_{^{56}\rm Ni}} \times \exp\left(-t/\tau_{^{56}\rm Co}\right). \quad (1)$$

Thus, $M_{\rm Ni}$ is estimated by performing a linear fit to the logarithm of the bolometric luminosity during the radioactive tail ($t > t_{\rm f}^{*}$):

$$\log_{10} L_{\rm Bol.}[\rm erg/s] = 43.18 + \log_{10} M_{\rm Ni}[\rm M_\odot] - \frac{t[\rm d]}{255.6}. \quad (2)$$

This provides a direct measurement of $M_{\rm Ni}$, one of the four key physical parameters of these SNe, effectively reducing the dimensionality of the inference problem from four free parameters to three.

To constrain the remaining parameters – E, $M_{\rm ej}$, and R_0 – we generally adopted the following system of scaling relations[3]:

$$\begin{cases} E &= (1.3\ \rm foe) \times \left(\frac{\bar{t}_{\rm M}}{94\ \rm d}\right)^2 \times \left(\frac{v_{\rm M}}{2145\ \rm km/s}\right)^3 \\ M_{\rm ej} &= (16\ \rm M_\odot) \times \left(\frac{\bar{t}_{\rm M}}{94\ \rm d}\right)^2 \times \left(\frac{v_{\rm M}}{2145\ \rm km/s}\right) \\ R_0 &= (3 \times 10^{12}\ \rm cm) \times \left(\frac{t_{\rm m}}{8.7\ \rm d}\right)^2 \end{cases}. \quad (3)$$

This system relies on two characteristic times ($t_{\rm m}$ and $\bar{t}_{\rm M}$) linked to the photometric evolution, and on the velocity $v_{\rm M}$, which can be measured from at least one spectrum around peak luminosity (close to $\bar{t}_{\rm M}$) or from multiple spectra obtained near that epoch. Following Paper I, $v_{\rm M}$ can be derived from the blueshift of the Fe II 5619 Å P-Cygni absorption, which remains approximately constant around the LC peak. However, the scaling relations of system (3) can only be applied when at least one spectroscopic measurement of the velocity around maximum light is available. Since this is not always the case, in order to characterize SNe lacking spectroscopic coverage, SuperBAM also allows the use of purely photometric scaling relations to define the priors, under the assumption that $v_{\rm M} \propto L_{\rm M}^{1/2}/\bar{t}_{\rm M}$ (similarly as seen in Paper I), where $L_{\rm M} = L_{\rm Bol.}(\bar{t}_{\rm M})$ is the bolometric luminosity at $\bar{t}_{\rm M}$. This assumption is specifically valid for type II SNe whose emission during the recombination phase can be approximated by that of a blackbody with a nearly constant temperature equal to the hydrogen recombination one (see Paper I; Paper II, and references). Under this hypothesis, the first two equations of system (3) can be rewritten as:

$$\begin{cases} E &= (1.3\ \rm foe) \times \left(\frac{\bar{t}_{\rm M}}{94\ \rm d}\right)^{-1} \times \left(\frac{L_{\rm M}}{8.6\times10^{42}\ \rm erg\ s^{-1}}\right)^{3/2} \\ M_{\rm ej} &= (16\ \rm M_\odot) \times \left(\frac{\bar{t}_{\rm M}}{94\ \rm d}\right) \times \left(\frac{L_{\rm M}}{8.6\times10^{42}\ \rm erg\ s^{-1}}\right)^{1/2} \end{cases}. \quad (4)$$

These alternative relations, although having the advantage of not relying on spectroscopic data, are typically affected by larger uncertainties due to the relative errors on luminosity (generally higher than those on velocity), as well as by the assumption of a common recombination temperature among different SNe. Nevertheless, they represent a valid and practical option for the construction of priors when spectroscopic information is unavailable.

In both cases, to incorporate this prior information on the physical parameters into the Bayesian framework, we define a probability distribution function (PDF) for each parameter. For $M_{\rm Ni}$, we adopt a Gaussian PDF with mean $\langle M_{\rm Ni}\rangle$ equal to the value obtained from the best-fit of the radioactive tail, and a standard deviation $\delta M_{\rm Ni}$ derived from the weighted fit uncertainties. For the remaining parameters (E, $M_{\rm ej}$, and R_0), the prior PDFs are obtained by combining skew-normal distributions (e.g., Ashour & Abdel-hameed 2010), modified to ensure support on positive values. These distributions are constructed from the measured features ($t_{\rm m}, \bar{t}_{\rm M}, v_{\rm M}, L_{\rm M}$) and their uncertainties, and subsequently mapped into the physical parameter space through the scaling relations of Eq. (3) (or 4). The full procedure is presented in Appendix A.

2.1.2. Likelihood definition

SuperBAM's likelihood function is designed to compare the observed bolometric LC data ($t^{\rm Obs.}$, $L_{\rm Bol.}^{\rm Obs.}$, $\pm\Delta L_{\rm Bol.}^{\rm Obs.}$) with the luminosity predicted by the analytical model of Paper II ($L_{\rm SN}$). In particular, this likelihood function considers only LC observations taken later than 30 days after explosion (i.e., $t^{\rm Obs.} > 30$ d), so that the inference of the main physical parameters relies exclusively on the morphology of the secondary peak, without being significantly affected by early-time luminosity contributions (e.g., optical thin shell or CSM interaction, see also Paper II).

To improve the efficiency of the model–data comparison, SuperBAM's likelihood works with dimensionless functions and variables. For this reason, the observed luminosity is normalized to the radioactive luminosity from ^{56}Ni decay expressed by Eq. (1). For each LC point, the normalized luminosity is defined as:

$$\bar{L}^{\rm Obs.} = \frac{L_{\rm Bol.}^{\rm Obs.}}{L_{\rm Ni}(t^{\rm Obs.})}, \quad (5)$$

where $L_{\rm Ni}(t)$ is computed assuming an ejected nickel mass equals to $\langle M_{\rm Ni}\rangle$, as estimated from the prior constraints (Sect. 2.1.1).

On the modeling side, this normalization has the key advantage of removing the explicit dependence on the ^{56}Ni mass, thereby reducing the number of free parameters in the normalized luminosity predicted by the model. The latter, $\bar{L} = L_{\rm SN}/L_{\rm Ni}$, is defined as the ratio between Eq. (58) of Paper II and Eq. (1). When expressed in terms of the dimensionless time coordinate $y = t/\tau_{^{56}\rm Co}$, $\bar{L}$ takes the following form:

$$\bar{L}(y) = \frac{[(y - y_i) \times H(y, y_i) + y_i]^2 \times e^{y+k_2}}{\lambda\, k_1^2\, (e^{k_2} - 1)} + \frac{e^{k_2\,(1-z^3)} - 1}{e^{k_2} - 1}, \quad (6)$$

where (y_i, λ, k_1, k_2) are the set of dimensionless model parameters and $z(\equiv x_i)$ is the comoving coordinate of the wave-front of cooling and recombination (WCR). Here, $H(y, y_i)$ denotes the Heaviside function, equal to one if $y > y_i$ and zero otherwise. Unlike the variable change adopted in Paper II for Eq. (58), the time coordinate used here (y) is independent of the SN timescale t_a, leading to a direct dependency of $y_i = t_i/\tau_{^{56}\rm Co}$ from progenitor radius. So the dimensionless parameters can be related to the

[3] The first two scaling equations in Eq. (3) are the same as in Eq. (4) of Paper I, while the third replaces Eq. (15) of the same work. Instead of relying on $L_{\rm min}$, $t_{\rm M}$, and $v_{\rm M}$, it directly relates the progenitor radius to $t_{\rm m}$, based on the proportionality derived in their Eq. (9). This assumes that t_i (the onset of recombination) coincides with the pre-peak luminosity minimum. Although Paper II has shown that this is not always strictly valid (particularly in cases where a thin shell or CSM interaction modifies the early luminosity) this relation is nonetheless simple and robust enough to provide useful prior information on R_0, while allowing sufficient flexibility for posterior inference.

physical SN quantities through the following scaling relations:

$$\begin{cases} y_i &= 8.15 \times 10^{-2} \times \left(\frac{R_0}{3\times10^{12}\,\mathrm{cm}}\right)^{1/2} \\ \lambda &= 5.02 \times \frac{M_{\mathrm{Ni}}}{7.4\,\mathrm{M}_\odot} \times \left(\frac{M_{\mathrm{ej}}}{16\,\mathrm{M}_\odot}\right)^{-1/2} \times \left(\frac{E}{1.3\,\mathrm{foe}}\right)^{-1/2} \\ k_1 &= 1.35 \times \left(\frac{E}{1.3\,\mathrm{foe}}\right)^{-1/4} \times \left(\frac{M_{\mathrm{ej}}}{16\,\mathrm{M}_\odot}\right)^{3/4} \end{cases}. \tag{7}$$

The remaining parameter k_2 depends only on the mixing of ^{56}Ni. In this work, we adopt the fixed value $k_2 = 32.87$ for all 1987A-like SNe, corresponding to a configuration in which 95% of the nickel mass is confined within 45% of the ejecta radius, assuming an exponential distribution (see Paper II). The effects of varying this parameter and a comparison with other models are discussed in Appendix B. With this formulation, the WCR evolution is governed by the following differential equation [cf. Eq. (54) in Paper II]:

$$\frac{dz^4}{dy} = -\frac{2}{y}\left[z^4 + \frac{y^2}{k_1^2}z^2 - \lambda \times e^{-y} \times \left(1 - e^{-k_2 z^3}\right)\right], \tag{8}$$

with boundary condition $z(y_i) = 1$.

Hence, once the boundary conditions are specified, the model luminosity $\bar{L}_{\mathrm{Mod.}} = \bar{L}(y; y_i, \lambda, k_1)$ depends on the three parameters (y_i, λ, k_1). These, together with the variance σ that accounts for intrinsic model uncertainties, define the parameter set θ of the likelihood function:

$$P(\bar{L}|\theta) = \frac{1}{\sqrt{2\pi}} \times \prod_{\mathrm{Obs.}} \frac{1}{\sqrt{(\sigma^{\mathrm{Obs.}})^2 + \sigma^2}} \times \exp\left\{-\frac{\left[\log \bar{L}^{\mathrm{Obs.}} - \log \bar{L}_{\mathrm{Mod.}}(y^{\mathrm{Obs.}}; k_1, \lambda, y_i)\right]^2}{2[(\sigma^{\mathrm{Obs.}})^2 + \sigma^2]}\right\}, \tag{9}$$

where $y^{\mathrm{Obs.}} = t^{\mathrm{Obs.}}/\tau_{^{56}\mathrm{Co}}$, $\sigma^{\mathrm{Obs.}} = \Delta \log \bar{L}^{\mathrm{Obs.}} = \Delta L^{\mathrm{Obs.}}/L^{\mathrm{Obs.}}$ is the error deviation linked to the observations, and σ represents a systematic uncertainty term that is used to capture extra variance in the data, arising from unmodeled variability or other sources of systematic error in the model. The likelihood function thus provides the statistical framework to compare observations and model predictions in terms of normalized luminosity. To achieve a consistent inference on the progenitor and explosion properties, it is then combined with the prior distributions introduced in Sect. 2.1.1, leading to the definition of the posterior probability distribution discussed in the next section.

2.1.3. Posterior exploration

The likelihood function is defined in terms of the parameter set $\theta = (y_i, \lambda, k_1, \sigma)$. To express the posterior consistently in this parameter space, the priors – originally formulated for the physical quantities $(E, M_{\mathrm{ej}}, R_0)$ – must be transformed accordingly. The use of θ instead of the direct physical parameters has the practical advantage that each of the three dimensionless parameters (y_i, λ, k_1) affects the WCR evolution in an independent way (cf. Eq. (8)). As a result, the LC model depends on them without strong internal degeneracies, unlike the case of the physical triplet E, M_{ej} and R_0 (see also Paper II, for a detailed discussion of degeneracy in 87A-like events). Following the procedure described in Appendix A, the prior PDFs ($\mathrm{PDF}^{\mathrm{Pr.}}$) for the dimensionless parameters can be constructed from those of $(E, M_{\mathrm{ej}}, R_0)$ through the combination of Eqs. (3) (or (4)) and (7). This yields:

$$\begin{aligned} &y_i \propto t_{\mathrm{m}}, \qquad \lambda \propto M_{\mathrm{Ni}} \times t_{\mathrm{M}}^{-5/2} \times v_{\mathrm{M}}^{-1}, \qquad k_1 \propto t_{\mathrm{M}}^{3/2} \\ &\quad \text{or} \qquad \lambda \propto M_{\mathrm{Ni}} \times t_{\mathrm{M}}^{-3/2} \times L_{\mathrm{M}}^{-1/2}. \end{aligned} \tag{10}$$

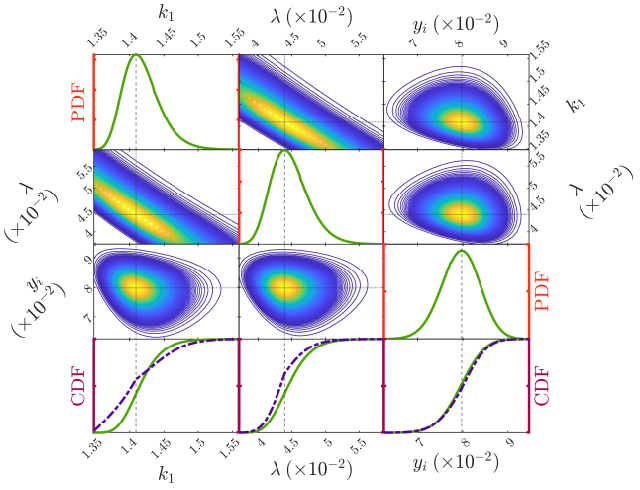

Fig. 2. Mosaic of $P(\theta|\bar{L})$ plots for SN 1987A. The color density maps show 2D slices of the log-posterior distribution with σ fixed, while two modeling parameters vary at a time. The diagonal panels display the posterior PDFs along each parameter axis, keeping the other parameters fixed at their best-fit values. The lower row shows the cumulative distribution function (CDF) for each parameter axis (solid line), compared to the CDF integrated on the entire space (dotted line).

The prior distribution for the modeling parameter set can then be written as:

$$P(\theta) = \mathrm{PDF}^{\mathrm{Pr.}}(y_i) \times \mathrm{PDF}^{\mathrm{Pr.}}(\lambda) \times \mathrm{PDF}^{\mathrm{Pr.}}(k_1) \times \mathrm{PDF}^{\mathrm{Pr.}}(\sigma), \tag{11}$$

where $\mathrm{PDF}^{\mathrm{Pr.}}(\sigma)$ is taken as a normal distribution with mean and variance estimated from the observed scatter $\sigma^{\mathrm{Obs.}}$. Finally, the posterior distribution is obtained as the product of likelihood and prior, up to a normalization factor N_{Norm}:

$$P(\theta|\bar{L}) = N_{\mathrm{Norm.}} \times P(\bar{L}|\theta) \times P(\theta). \tag{12}$$

The combination of Bayesian statistics with the efficiency of the analytic approach allows us to explore nearly the entire support of the posterior probability, thus distinguishing local maxima from the global one (see Fig. 2). SuperBAM implements an exploratory algorithm based on the Hamiltonian Monte Carlo (HMC) Sampler[4], which identifies the parameter vector $\theta^M = (y_i^M, \lambda^M, k_1^M, \sigma^M)$ that maximizes the posterior $P(\theta|\bar{L})$. By varying one parameter at a time, the posterior PDFs ($\mathrm{PDF}^{\mathrm{Po.}}$) can be derived around θ^M through renormalization (see the diagonal panels in Fig. 2):

$$\mathrm{PDF}^{\mathrm{Po.}}(\theta_i) = K_i \times P\left(\theta_i, \theta^M_{j\neq i} \mid \bar{L}\right), \tag{13}$$

where $K_i^{-1} = \int_0^{+\infty} \mathrm{PDF}^{\mathrm{Po.}}(\theta_i)\, d\theta_i$ is the normalization constant. Once the posterior PDFs for $(k_1^M, \lambda^M, y_i^M)$ are obtained, the corresponding PDFs of the physical explosion parameters $(E, M_{\mathrm{ej}}, R_0)$ can be reconstructed by applying the inverse transformations of Eq. (7), as described in Appendix A.

It should be noted, however, that these posterior PDFs are derived in a univariate way (i.e., along single axes). This approach may underestimate modeling uncertainties, since off-axis correlations between parameters are not fully captured. For instance, inspection of the k_1–λ plane reveals a non-negligible

[4] The HMC algorithm is a Markov Chain Monte Carlo technique that generates random samples to efficiently explore and maximize a multi-parametric distribution. See also the MatLab documentation for details.

covariance, intrinsic to the model due to their product entering the normalized luminosity in Eq. (6). As illustrated by the difference between the CDFs along the axes and over the full space (Fig. 2), the broader multidimensional distributions highlight the need to account for covariance-driven uncertainties. To address this limitation, SuperBAM employs a Monte Carlo (MC) procedure that randomly generates 10^4 triplets of modeling parameters (y_i, λ, k_1) around the HMC best-fit solution θ^M, fixing $\sigma = \sigma^M$. For each triplet, the posterior probability value is computed and used as a statistical weight, naturally decreasing with distance from the optimum. From this weighted sample of parameter triplets, expectation values and variances are derived for both the modeling parameters and, through the inverse transformations of Eq. (7), for the physical parameters $(E, M_{\rm ej}, R_0)$.

2.2. Validation test

To validate our approach, we apply SuperBAM to the previously published LCs of SN 1987A (Catchpole et al. 1987), SN 2009E (Pastorello et al. 2012), and OGLE-14 (Terreran et al. 2017), shown in Fig. 1, and compare the results with the HM from Pumo & Zampieri (2011)'s post-explosive model (see Table 1 of Paper II, and references therein). As a consequence, the temporal sampling of the bolometric LCs reflects the reconstruction methods used in the original works and may slightly differ from that obtained with our own bolometric reconstruction technique (see also Sect. 3.1). Based on the procedure outlined in Section 2.1, SuperBAM provides an initial estimate from the priors for E, $M_{\rm ej}$, R_0, and $M_{\rm Ni}$, as well as two posterior estimates of E, $M_{\rm ej}$, and R_0 obtained through different approaches. The first, referred to as the posterior best model, corresponds to the parameter configuration that maximizes the posterior probability (i.e., the mode of the distribution), derived using the HMC sampler; the associated uncertainty is estimated from a univariate analysis of the posterior. The second, instead, is obtained through a MC simulation, yielding the mean values and standard deviations of the physical parameters over the multidimensional posterior support. These two posterior estimates are consistent with each other within their respective error bars, demonstrating SuperBAM's ability to converge toward coherent and more precise modeling results compared to those obtained from the priors through the scaling relations (see Table 1).

As the output of SuperBAM, we adopt the best-fit model obtained with the HMC-Sampler, while assigning uncertainties derived from the MC approach. This choice combines the advantage of a model that best reproduces the observed data with error estimates that account for multidimensional parameter correlations.

When comparing the SuperBAM results with the HM, we find that the results are fully consistent within the errors, with the only exception of the energy for SN 2009E (about a factor two higher). This offset in the explosion energy is present in all SNe and it is especially evident for SN 2009E and OGLE-14. This systematic discrepancy can be traced back to the intrinsic assumptions of semi-analytic models. Indeed, unlike hydrodynamical simulations, our model adopts a uniform density profile for the ejecta. As already discussed in previous works, this simplification leads to an overestimate of the energy budget because more mass is effectively concentrated in the fast-moving outer layers, increasing the kinetic energy content. This behavior was noted for OGLE-14 by Terreran et al. (2017), where the semi-analytic model of Zampieri et al. (2003) yielded an explosion energy ~70% larger than the HM estimate, precisely because the early acceleration phase of the ejecta is not accounted for.

Table 1. Results of the validation test.

Par.	Method	SN 1987A	SN 2009E	OGLE-14
E [foe]	Pr.	1.4 ± 0.9	0.8 ± 0.2	18 ± 11
	Po.	1.6 ± 0.2	1.1 ± 0.1	20 ± 5
	MC	1.7 ± 0.4	1.2 ± 0.2	21 ± 7
	HM	1.3 ± 0.1	0.6 ± 0.2	12^{+13}_{-6}
$M_{\rm ej}$ [$M_\odot$]	Pr.	16 ± 5	15 ± 2	43 ± 16
	Po.	18 ± 1	23 ± 1	46 ± 5
	MC	19 ± 3	24 ± 2	48 ± 8
	HM	16 ± 1	19 ± 3	60^{+42}_{-16}
R_0 [10^{12} cm]	Pr.	4 ± 3	4 ± 4	25 ± 21
	Po.	2.9 ± 0.3	4.6 ± 0.2	25 ± 3
	MC	2.8 ± 0.3	4.5 ± 0.5	27 ± 4
	HM	3.0 ± 0.9	7 ± 1	38^{+8}_{-10}
$M_{\rm Ni}$ [$10^{-2}\,M_\odot$]	Pr.	7.4 ± 0.9	3.9 ± 0.2	42 ± 13
	HM	7 ± 1	4 ± 1	47 ± 2

Notes. Comparison of priors (Pr.), best model posterior (Po.), and MC results with those from numerical HM for SN 1987A, SN 2009E, and OGLE-14.

A similar result was reported for SN 2009E in Pastorello et al. (2012), where the same semi-analytic approach produced an $M_{\rm ej} \sim 26\,M_\odot$ and an $E \sim 1.3$ foe, again exceeding HM estimates due to the uniform density assumption. SuperBAM mitigates part of this bias, as it accounts for the effect of ^{56}Ni heating on the recombination process. As noted by Pastorello et al. (2012), neglecting the non-uniform distribution of ^{56}Ni leads to an underestimate of its contribution at late photospheric phases, forcing the model to invoke a more massive envelope to sustain the recombination. By incorporating this effect, SuperBAM achieves results that converge more closely to HM values, especially for the ejecta mass. Smaller differences are found in the initial radius. In our framework, the uniform-density assumption tends to confine the ejecta more tightly at early times, leading to slightly smaller radii than those inferred from HM. This discrepancy increases with ejecta mass, but in the case of OGLE-14 the results remain consistent within the error bars.

Finally, it is important to emphasize that the ^{56}Ni mass derived by SuperBAM from the LC tail (cf. Eq. (2)), corresponds to the amount of nickel present in the ejecta at late times. This represents a lower limit compared to HM results, which include the fraction of nickel that falls back onto the compact remnant. Consequently, our ^{56}Ni masses are systematically lower than those obtained with HM. In summary, SuperBAM offers a fast and physically consistent way to characterize 1987A-like SNe, providing results comparable to HM, while significantly reducing the computational time. This makes SuperBAM particularly well suited for the analysis of large SN samples.

3. The sample of 87A-like SNe

Over the last two years, the number of published 87A-like SNe has nearly doubled, largely thanks to the efforts of wide-field surveys such as ZTF/CLU (Sit et al. 2023). In Paper I, a sample of 14 SNe 1987A-like was analyzed using the approach of scaling relations, relying on bolometric LCs and velocity data already available in the literature. In this work, we expand this sample to nearly double its size by homogeneously reconstructing the bolometric LCs, estimating line velocities and their pseudo-equivalent widths (pEWs) from peak spectra, and applying the

Table 2. Sample of 1987A-like SNe and key information used for the spectrophotometric analysis.

SN Name	Explosion Epoch [MJD]	Host Galaxy Name	Redshift (z)	m-M [mag]	A_V(tot) [mag]	12+log(O/H)[a]	Ref.
SN 1987A	46849.8	LMC	0.0009	18.5 ± 0.1	0.600	8.37 ± 0.06	1,2
SN 1998A	50763.3	IC 2627	0.0072	32.2 ± 0.3	0.383	8.68 ± 0.06	3
SN 2000cb	51651.1	IC 1158	0.0064	32.7	0.353	8.45 ± 0.06	4
SN 2004ek	53250.5	UGC 724	0.0173	34.4 ± 0.3	0.530	8.59	5
SN 2004em	53263.3	IC 1303	0.0149	33.9 ± 0.3	0.298	8.56 ± 0.11	5
SN 2005ci	53512.4	NGC 5682	0.0076	32.8	0.089	8.31 ± 0.04	5
SN 2006V	53748.0	UGC 6510	0.0158	34.4 ± 0.8	0.090	8.35 ± 0.11	6
SN 2006au	53794.0	UGC 11057	0.0099	33.4 ± 0.8	0.970	8.49 ± 0.12	6
SN 2009E	54824.5	NGC 4141	0.0063	32.4 ± 0.4	0.124	8.22 ± 0.08	7
SN 2009mw	55174.5	ESO 499-G005	0.0143	33.5 ± 0.2	0.167	8.32	8
PTF12gcx	56081.3	SDSS J154417.02+095743.8	0.0450	36.5 ± 0.2	0.140	8.52 ± 0.18	5
PTF12kso	56175.0	Anon.	0.0300	35.6 ± 0.2	0.184	$\lesssim$8.04	5
OGLE-14	56861.1	Anon.	0.1225	38.8	0.170	8.36 ± 0.10	9
SN Refsdal	56968.9	Anon.-Lensed[b]	1.4910	45.2 ± 0.1	0.310	8.3 ± 0.1	10
DES16C3cje	57670.2	PGC324331	0.0618	37.2	0.527	<8.19 ± 0.02	11
SN 2018cub	58216.3	WISEA J150541.98+604751.4	0.0440	36.5	0.047	8.43	12
SN 2018ego	58248.3	2MASX J15525218+1958107	0.0375	36.2	0.144	7.60	12
SN 2018imj	58380.0	IC0454	0.0132	33.7 ± 0.2	0.627	8.19	11
SN 2018hna	58411.3	UGC 07534	0.0024	30.5 ± 0.3	0.028	8.14 ± 0.02	13
SN 2019bsw	58482.7	WISEA J100506.20-162425.1	0.0295	35.6	0.140	NaN	12
SN 2020faa	58926.0	WISEA J144709.05+724415.5	0.0411	36.2 ± 0.2	0.067	8.40 ± 0.1	14,15
SN 2020oem	58982.8	WISEA J152729.72+034646.8	0.0424	36.4	0.139	8.34	12
SN 2020abah	59175.5	CGCG 127-002	0.0301	35.7	0.065	8.42	12
SN 2021zj[c]	59224.4	SDSS J111632.91+290546.5	0.0460	36.6 ± 0.1	0.038	NaN	12,16
SN 2021mju	59287.5	WISEA J164148.29+192203.6	0.0283	35.5	0.210	8.14	12
SN 2021skm	59389.4	2MASX J16165615+2148359	0.0315	NaN	0.222	8.30	12
SN 2021wun	59425.2	SDSS J154631.94+252545.5	0.0228	35.1	0.128	8.17	12
SN 2021aatd	59493.5	GALEXASCJ005904.40-001210.0	0.0152	34.2	0.078	NaN	17

Notes. (1) Pun et al. (1995); (2) Catchpole et al. (1987); (3) Pastorello et al. (2005); (4) Kleiser et al. (2011); (5) Taddia et al. (2016); (6) Taddia et al. (2012); (7) Pastorello et al. (2012); (8) Takáts et al. (2016); (9) Terreran et al. (2017); (10) Kelly et al. (2016); (11) Gutiérrez et al. (2020); (12) Sit et al. (2023); (13) Singh et al. (2019); (14) Yang et al. (2021); (15) Salmaso et al. (2023); (16) Jacobson-Galán et al. (2024); (17) Szalai et al. (2024). Column 2 lists the estimated explosion epoch, computed as the midpoint between the last non-detection and the discovery date. The host galaxy name is given in Column 3 (with "Anon." indicating anonymous hosts), followed by the redshift (z in Col. 4) and the distance modulus (m-M in Col. 5; when not reported in the cited references, values are taken from the NASA/IPAC Extragalactic Database). Columns 6 and 7 report the total visual extinction, A_V (Milky Way + host contribution, following Schlafly & Finkbeiner 2011), and the oxygen abundance at the SN site [12+log(O/H)], respectively. The final column lists the main references from which these quantities, as well as the multi-band photometric data and spectra used in this work, are collected. Entries marked as "NaN" indicate that the corresponding information is not available in the literature. [(a)] Unless otherwise specified in the cited references, the oxygen abundances are derived using the N2 diagnostic (see Taddia et al. 2013). [(b)] SN Refsdal, discovered in the MACS J1149+2223 galaxy cluster, was observed as a strongly lensed SN with multiple resolved images (Kelly et al. 2016). Among the four images, this work focuses on S2, assuming a magnification factor of $\mu = 15$ (Grillo et al. 2016). [(c)] No public spectra are available for SN 2021zj during the secondary peak phase. Classified as a young SN II by Smith et al. (2021), it showed flash ionization signatures in the early spectra.

SUPERBAM procedure to derive the physical properties at the explosion.

To this aim, we performed a systematic search through the literature of the past three decades, selecting the best-observed long-rising type II SNe according to the following criteria:

- Multi-band photometric coverage (at least three filters) starting no later than $\bar{t}_M - 40$ d and extending through the end of the recombination phase (t_f^*) with at least one point on the ^{56}Ni tail. This allows us to reconstruct the bolometric LC and constrain priors such as the ^{56}Ni mass.
- Reliable estimates of distance (or redshift) and extinction are required. It is necessary to correct both spectra and photometry before deriving bolometric LCs and velocities.

Both SUPERBAM and alternative modeling approaches require these conditions to be applied; otherwise, the analysis cannot be considered reliable (e.g., Martinez & Bersten 2019). Following these criteria, we selected a sample of 28 long-rising type II SNe published before 2025. The list reported in Table 2 includes, for each of these events, the estimated explosion epoch (which is not a free parameter of the fit, but is fixed as the midpoint between the last non-detection and the discovery date), the host galaxy with its distance modulus, the adopted redshift, the total visual extinction, and the environmental metallicity in terms of oxygen abundance [12+log(O/H)], along with the main bibliographic references from which this information is taken.

The collection of multi-band photometric data for each SN enables the reconstruction of their bolometric LCs. In addition to the datasets published in the references listed in Table 2, we also include, where available, photometry from the ATLAS (Asteroid Terrestrial-impact Last Alert System; see, e.g., Tonry et al. 2018). Spectroscopic data are gathered from the same cited works, selecting spectra obtained near the luminosity

peak (see Table C.2 for acquisition dates and epochs of the spectra considered for each SN). These spectra are used to measure photospheric velocities and line equivalent widths, providing complementary constraints on the ejecta composition and kinematics. Although, no public spectra are available for SN 2021zj during the peak stage, its modeling was carried out by SuperBAM using the full photometric scaling relations system in Eq. (4). However, this object is not included in the spectroscopic analysis made for the other 1987A-like SNe in the sample.

3.1. Bolometric luminosity

For the computation of bolometric luminosity, all available multi-band photometry from the literature has been re-analysed in a homogeneous way, ensuring a consistent procedure for the construction of bolometric LCs. In particular, we apply SuperBol procedure for the bolometric integration of the spectral energy distribution (SED) described by Nicholl (2018). In addition, the multi-band LCs are first reconstructed in time using GPR interpolation, and extrapolated under the constant-color assumption[5]. The use of GPR provides synthetic photometric points at missing epochs, effectively increasing the number of multi-band observations and allowing for virtually simultaneous coverage across filters[6]. This interpolation yields a denser bolometric sampling while preserving consistency with curves derived from real data within the uncertainties[7]. In addition to photometry, information on distance and extinction is required. For SNe with $z > 0.01$, distances are derived from the redshift, assuming $\Omega_\Lambda = 0.685$, $\Omega_M = 0.315$ and the Hubble-Lemaıtre constant equals to $H_0 = 67.4\,\mathrm{km\,s^{-1}\,Mpc^{-1}}$ (e.g., Planck Collaboration VI 2020). For nearby SNe, where peculiar motions can dominate over the Hubble flow, we adopt published distance moduli (Table 2). In the case of the gravitational lensed SN Refsdal, we also correct the observed flux for the magnification lens factor $\mu = 15$ (e.g., Grillo et al. 2016, and references therein). The reddening correction is applied assuming the Cardelli et al. (1989) extinction law with $R_V = 3.1$, appropriate for the diffuse interstellar medium. The color excess $E(B-V)$, computed as the difference between observed and intrinsic colors, is then estimated from the total extinction as $E(B-V) = A_V/R_V$. Finally, no UV cut-off is applied to the SEDs. Although the early post-explosion phases (<10–20 d) might be affected by a significant drop in the UV flux, this effect is negligible for SNe II because of the hydrogen-rich, metal-poor nature of their ejecta (e.g., Gezari et al. 2008; Bufano et al. 2009), and is irrelevant for our analysis, which does not rely on the earliest epochs. However, the SED fitting is potentially affected by line blanketing[8].

The bolometric LCs obtained in this way are then used by SuperBAM to constrain the physical parameters of the explosions (see Sect. 4). As a preparatory step, however, the procedure also measures key morphological features of the LCs, reported in Table C.1, such as $M_{\rm Ni}$, $t_{\rm f}^*$ and $L_{\rm M}$ (see left panels of Fig. 3). The distribution of nickel masses, directly inferred from the radioactive tails, spans nearly an order of magnitude, from the $\sim$0.04 $\mathrm{M_\odot}$ of SN 2009E up to the 0.4–0.5 $\mathrm{M_\odot}$ measured for OGLE-14 and SN 2021zj. Grouping the sample according to $M_{\rm Ni}$ highlights three main subsets. Events with $M_{\rm Ni} < 0.1\,\mathrm{M_\odot}$, including SN 1987A and SN Refsdal, cluster around peak luminosities of $\sim 10^{42}\,\mathrm{erg\,s^{-1}}$ and recombination end times $t_{\rm f}^* \approx 100$–150 d. SNe with intermediate nickel masses (0.1–0.2 $\mathrm{M_\odot}$) reach higher peak luminosities, still consistent with the observed scaling, but in some cases show broader LCs, as for DES16C3cje, whose $t_{\rm f}^*$ exceeds 200 d. Finally, the most nickel-rich explosions ($M_{\rm Ni} > 0.2\,\mathrm{M_\odot}$) attain luminosities above $10^{43}\,\mathrm{erg\,s^{-1}}$, with OGLE14-73 representing the event with the brightest and broadest peak of the class. SN 2021zj and SN 2020faa also belong to this group, though they display a slow pre-maximum rise, with $t_{\rm m} \sim 40$–60 d, unlike OGLE14-73 where no early coverage is available. Across the entire sample, $L_{\rm M}$ shows a linear increase with $M_{\rm Ni}$, as illustrated in the left-up panel of Fig. 3. This trend has also been reported in broader samples of H-rich SNe (e.g., Martinez et al. 2022), and becomes particularly clear for 1987A-like SNe, in which the radioactive Ni-heating is more powerful than the ejecta recombination-cooling (i.e., where the Λ-term dominates; see Eqs. (67)–(68) in Paper II). However, events such as OGLE-14 and SN 2020faa exhibit luminosities significantly above the predicted trend, suggesting the contribution of additional energy sources that enhance the overall brightness. On the contrary, the same clear dependency on $M_{\rm Ni}$ is not observed for $t_{\rm f}^*$, which is more influenced by other properties of the explosion, deriving from its link with the diffusion and ejecta expansion rates ($t_{\rm f}^* \propto M_{\rm Ni}^{1/3} E^{-1/2} M_{\rm ej}^{5/6}$; cf. Eq. (76) of Paper II).

3.2. Spectroscopic features

The available SN spectra have been reduced and corrected for both reddening and redshift, thus placing them in the rest frame and recovering their intrinsic continuum shape. These corrections, applied consistently across the sample, allow a direct comparison of line profiles and velocities, providing essential constraints on the ejecta properties.

For this purpose, the *deredden* and *dopcor* tasks within the Image Reduction and Analysis Facility (IRAF; Tody 1986) are employed. After the corrections, the main absorption features typical of SNe 1987A-like are analyzed, with particular attention to the Balmer lines (Hα, Hβ) and metal lines such as Ba II-λ6142 and Fe II-λ5169. The minima of the P-Cygni absorption profiles are measured using Gaussian fits with the IRAF *splot* tool, in order to infer the expansion velocities from their Doppler shifts. Simultaneously, these fits provide the pEWs used to characterize line strengths and assess the relative contribution of different ions. The results of this analysis are summarized in Table C.2 and illustrated in the right panels of Fig. 3.

From a spectroscopic point of view, the majority of the SNe show broad P-Cygni Balmer profiles together with Fe II and Ba II features, which are particularly suited to trace the photospheric velocity. In our procedure, the photospheric velocity at peak ($v_{\rm M}$) adopted in the priors of SuperBAM is taken from

[5] The constant-color refers to a temporal extrapolation technique in which missing-band fluxes are estimated by preserving the color difference measured at the nearest epoch with multi-band coverage (see Nicholl 2018).

[6] In wide-field surveys (e.g., LSST), multi-band photometry is typically obtained on different nights, depending on the observing strategy (Bianco et al. 2021). In such cases, GPR is particularly effective.

[7] See also Fig. 4.2 in Cosentino (2024).

[8] As in normal Type II SNe, the SEDs of 1987A-like events can be affected by line blanketing in the blue bands (e.g., Kasen & Woosley 2009; Pastorello et al. 2012). We verified that recomputing the bolometric LC of SN 1987A with and without the U and B bands leads to differences of ~5–20%, comparable to the intrinsic uncertainties of the blackbody fitting procedure. Bolometric LCs obtained by integrating all available bands and extrapolating to missing regions using a blak-body fit provide robust estimates of the total emergent luminosity (e.g., Lyman et al. 2014; Taddia et al. 2016).

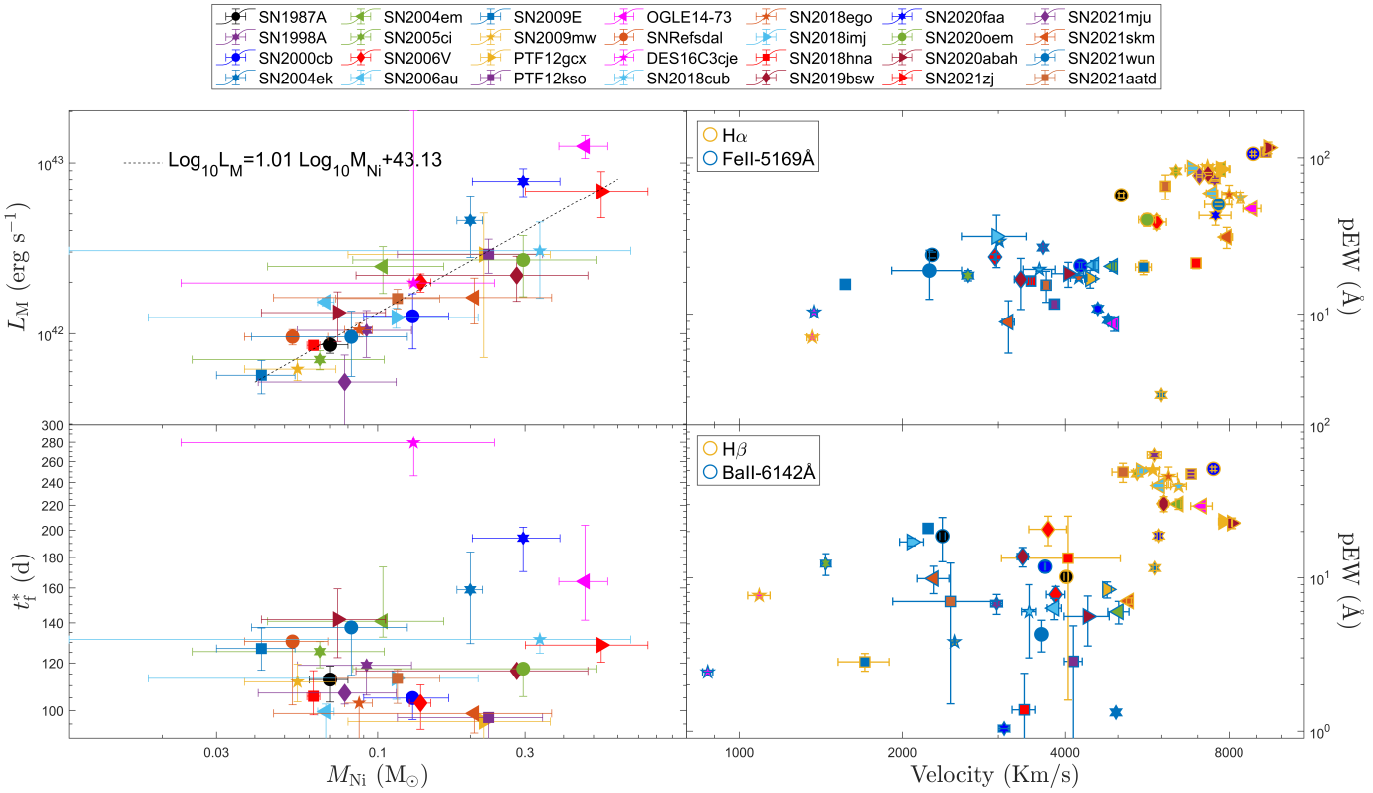

Fig. 3. Observational properties derived from the bolometric LCs and spectra of the SN sample. Top left: Distribution of the peak luminosity $L_{\rm M}$ as a function of the ^{56}Ni mass estimated from the radioactive tail fit. The trend line is obtained through a linear regression $\log_{10} L_{\rm M}$-$\log_{10} M_{\rm Ni}$; the correlation is highly significant (p-value $\ll 0.01$ and Pearson coefficient of 0.89). Bottom left: Distribution of t_f^* versus the ^{56}Ni mass for the same SN sample. Top right: pEWs as a function of expansion velocities for the Hα and Fe II lines, for the SNe with available data. The color and shape of the markers follow the top legend, while the marker border indicates the line type according to the internal legend. Bottom right: Same as the top-right panel, but for the Hβ and Ba II lines.

the Fe II velocity, which is available for the large majority of the sample. When Fe II is not detected, the Ba II velocity is used instead, and in the few cases where neither of these lines is measurable (e.g., SN Refsdal and SN 2020oem) the Hα velocity is employed, rescaled by a factor of 2 to account for the systematic offset between hydrogen and metal lines. Indeed, Balmer lines yield expansion velocities of 6000–9000 km s^{-1}, systematically higher (by a factor of 1.5–2.5) than those derived from metal lines (2000–5000 km s^{-1}). This difference originates from the fact that Balmer transitions are mostly shaped by photoionization and recombination processes in the outer ejecta layers, where the gas is only partially ionized and expands at higher velocities. Conversely, ionized metal lines require higher temperatures to sustain the proper ionization state, and become more prominent where the abundance of heavy elements is larger, i.e., in deeper and slower-moving regions of the photosphere. The smaller velocity offset between Hβ and Ba II supports this interpretation, since the Hβ formation region lies deeper than that of Hα and requires a higher excitation energy to populate the $n = 4$ level. Only a few objects deviate from these general trends, such as SN2009E and SN2005ci, which display unusually large offsets between Balmer and metal velocities.

As for pEWs, the Balmer lines generally exceed the strength of metal features by factors of 5–10. A noteworthy case is DES16C3cje, whose narrower Hα profile and weaker relative pEW suggest a non-standard post-explosion scenario (see also Gutiérrez et al. 2020). At peak phase, Fe II pEWs across the whole sample remain relatively uniform, typically in the range of 10–30 Å. In contrast, Ba II displays a much larger scatter, with values spanning from a few Å (e.g., SN 2018hna) up to ∼10 Å or more (e.g., SN 1987A and SN 2009E). Previous studies had suggested the existence of two distinct subgroups of 87A-like SNe based on Ba II strength (e.g., Takáts et al. 2016); however, in our extended sample the distribution appears more continuous, with several events occupying intermediate values.

In addition, a possible anti-correlation between the velocity of the Ba II line and its pEW is hinted at in our data. Although the statistical significance of this trend is limited (see Sect. 4.2), it can be interpreted in terms of the ejecta density structure. In more compact explosions, where the ejecta expand less rapidly, the higher density in the line-forming regions favors stronger Ba II absorption (cf. Mazzali & Chugai 1995). Within this framework, SNe with lower Ba II velocities during the peak phase are naturally expected to display deeper Ba II lines. While the spectra considered here are all collected around the recombination peak phase, variations in the location and temperature of the Ba II formation region can also affect this line strength (e.g., Xiang et al. 2023). A systematic investigation of spectrophotometric dependencies, including the role of physical parameters, is deferred to Sect. 4.2.

4. Modeling long-rising SNe with SuperBAM

To explore the physical properties of the selected 1987A-like sample, we applied the SuperBAM procedure to the entire set of objects. As discussed in Sect. 2, the pipeline provides estimates of the explosion energy, ejecta mass, and progenitor radius (summarized in Table C.3), as well as the synthesized

^{56}Ni mass, the latter being directly constrained from the radioactive tail of the LC (Table C.1). By comparing the observed LCs with the simulated ones obtained from the models presented in Paper II and Popov (1993), and using the parameters derived by SuperBAM through scaling relations and HMC sampling, we can evaluate both the physical parameter inference and the capability of these models to reproduce the observed bolometric evolution (Fig. 4).

The Ni–free simulations of Popov (1993) systematically underestimate both the peak luminosity and the end of the recombination phase, owing to the absence of additional heating from radioactive ^{56}Ni in the ejecta. A direct comparison between the Popov (1993) and Paper II models therefore allows us to quantify the role of ^{56}Ni in shaping the LC morphology. Interestingly, this difference becomes progressively smaller in SNe with recombination onset later than ∼30 days, i.e., for progenitors with significantly larger initial radii (cf. Eq. (7)). As expected, the best-fit posterior models provide a significantly better agreement with the data compared to the priors, which generally capture the onset and termination of recombination but fail to accurately reproduce the luminous intensity.

Among the 28 SNe in the sample, ten show a reduced chi-squared[9] (χ^2_ν) above unity, while the others are well fitted within the observational uncertainties. A first group of events, including SN1987A, SN1998A, SN2000cb, SN2004em, SN2006V, SN2009E, SN2009mw, SN2018hna, and SN2021aatd, shows excellent agreement between models and observations (i.e., $\chi^2_\nu \sim 1$), indicating that the automatic procedure robustly recovers the main LC features. For SN 2006V and SN 2018hna, however, the statistical agreement is formally poorer (reduced $\chi^2_\nu \sim 2.3$–2.7), mainly because the exceptionally dense UV–NIR multi-band coverage yields very small bolometric uncertainties (∼0.02 dex). Rescaling the log10-luminosity error to more typical values (0.05 dex) would bring the χ^2_ν below unity, confirming the adequacy of the fit.

A second group, made by PTF12gcx, PTF12kso, DES16C3cje, SN 2018cub, SN 2018imj, SN 2020oem, SN 2020abah, SN 2021zj, SN 2021skm, and SN 2021wun, also yields apparently excellent fits. However, in some of these cases the error bars on the reconstructed bolometric flux are significantly large, that reduce the $\chi^2_\nu \lesssim 0.5$, limiting so the statistical robustness of the LC comparison and parameters inference.

Other SNe display discrepancies mainly due to limited temporal coverage or underestimated photometric errors. For instance, SN 2004ek, SN 2006au, and SN 2018ego suffer from sparse data and very small luminosity uncertainties, which drive the χ^2_ν to high values (grater than 3) despite an overall model-consistent evolution. SN Refsdal is fairly well reproduced around peak luminosity, but the lack of late–time data prevents a reliable constraint on the end of recombination. In some cases, the models clearly overfit or misinterpret parts of the LC. SN 2005ci shows spurious overfitting of the early rise, while SN2019bsw and SN 2021mju suffer from noisy data that lead the procedure to confuse the late plateau with the onset of the tail, introducing large uncertainties in all explosive parameters.

The two most luminous events in the sample, OGLE-14 and SN 2020faa ($L_{\rm M} \sim 10^{43}$ erg s^{-1}), both return reduced χ^2_ν values well above unity, highlighting the difficulty of reproducing the entire peak solely through the contribution of radioactive ^{56}Co. In OGLE-14, the higher χ^2_ν value is mainly due to the deviation seen at the end of recombination, which could be explained by a different ejecta density structure or an additional energy source placed inside. For SN 2020faa, the deviation is further supported by a change of slope in the nebular tail, suggesting the presence of an additional power source. A plausible interpretation is energy input from a hidden shock–powered mechanism, possibly magnetar–driven (see also Salmaso et al. 2023), contributing to the luminosity at nebular phases. Interestingly, DES16C3cje also deviates from the expected ^{56}Co decline rate and is instead compatible with the shallower slope expected from accretion–powered emission (Gutiérrez et al. 2020).

Finally, several SNe show an early–time luminosity excess (within ∼30 days of explosion) relative to the adopted model, which does not include contributions from thin-shell emission (see details in Paper II) or shock interaction with a dense CSM (e.g., Cosentino et al. 2025). Out of the 28 SNe analyzed, 13 exhibit this behavior, with particularly striking examples being SN2021zj and SN2021aatd. In SN2021zj, the interaction scenario is supported by the presence of narrow emission lines in the spectra (Jacobson-Galán et al. 2024), while in SN2021aatd no narrow features were detected beyond the first two days. However, the absence of narrow lines does not rule out CSM interaction as the underlying mechanism (e.g., Khatami & Kasen 2024, and references therein).

4.1. Physical properties of the 87A-like class

The physical parameters derived from the SuperBAM modeling for the 1987A-like sample are listed in Table C.3. When considered as a whole, they reveal a rather heterogeneous population, with asymmetric distributions in explosion energy and ^{56}Ni mass (see Fig. 5). In contrast, the distribution of ejecta masses is nearly symmetric, with the mean, median, and mode all close to ∼19 $M_\odot$. Explosion energies and ^{56}Ni masses, however, display a mode shifted toward lower values, with 8 SNe clustering below the sample averages. This points to the presence of two broad subgroups of 87A-like events: one characterized by modest energies (∼1.2 foe) and ^{56}Ni masses around 0.07 $M_\odot$ (including SN 1987A, SN 2009E, etc.), and another, more energetic, group peaking around 4 foe and ^{56}Ni masses above 0.11 $M_\odot$. About one quarter of the sample exhibits explosion energies exceeding 5 foe, reaching values that are difficult to reconcile with standard CC mechanisms (e.g., OGLE-14 and SN 2020faa).

By mapping energy, ejecta mass, and ^{56}Ni together, the extended sample allows us to better outline the parameter space of 1987A-like SNe. The resulting distribution appears continuous, but still allows events to be broadly grouped into two categories: a high-E, high-^{56}Ni subgroup with ejecta masses $\gtrsim$20 $M_\odot$ (e.g., OGLE-14), and another, more similar to SN 1987A, with lower ejecta masses (<20 $M_\odot$) and explosion energies spanning a wide range from ∼0.3 foe up to ∼2 foe, in line with the trends already reported in Paper I.

Similarly to ejecta masses, progenitor radii at the explosion time show a roughly symmetric distribution centered around (6−7)×10^{12} cm, but with two secondary tails: one at smaller radii of order 10^{12} cm, and another at larger radii, beyond 3×10^{13} cm.

[9] The reduced chi–squared is defined as

$$\chi^2_\nu = \nu^{-1} \times \sum_{\rm Obs.} \left[\left(L^{\rm Obs.}_{\rm Bol.} - L^{\rm Mod.} \right) / \Delta L^{\rm Obs.}_{\rm Bol.} \right]^2 ,$$

where $\nu = N^{\rm Obs.} - 4$ is the freedom degree depending on the number of bolometric observations $N^{\rm Obs.}$ after 30d since explosion, the sum is extended on these observed data ($L^{\rm Obs.}_{\rm Bol.}$, $\Delta L^{\rm Obs.}_{\rm Bol.}$), and $L^{\rm Mod.}$ are the corresponding model bolometric luminosities at $t^{\rm Obs.}$.

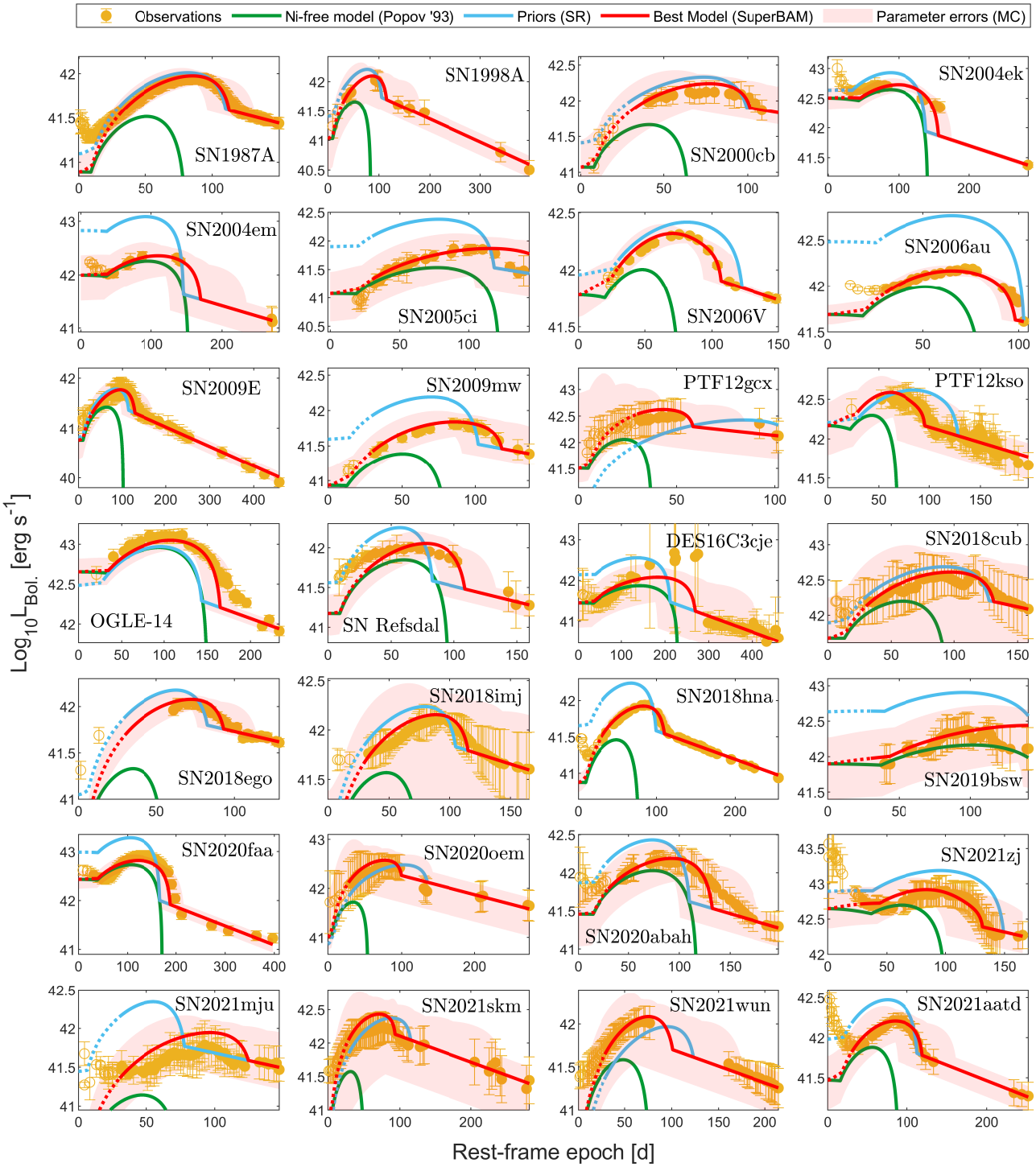

Fig. 4. Bolometric LC data for each SN in our sample. The name of each SN is indicated within its panel. The adopted explosion epochs ($t = 0$) are fixed from observational constraints (see Table 2). Along with the data, we present the synthetic LCs obtained from the analytical model described in Paper II. The parameters for these models were determined using the prior values given by the scaling relations, and the best-fit model obtained from SuperBAM analysis. The shaded region marks the LCs associated with the explored parameters within the error ranges of the MC method. Data earlier than 30 days are not included in the fitting procedure. For comparison, the synthetic LC of the nickel-free model by Popov (1993) is also included, calculated for the best-model parameters.

The low-radius tail includes events such as SN 2018ego, SN 2020oem, PTF12gcx, SN 2021mju, SN 2021skm, and SN 2021wun. However, these objects generally suffer from poor or noisy coverage in the early phases or near the end of recombination, which likely makes the radius estimates uncertain and possibly underestimated. Conversely, the high-radius tail contains several well-sampled and robustly modeled events (e.g., SN 2004em, SN 2004ek, OGLE-14, and SN 2021zj). Interestingly, the highest-radius events are also those with the largest explosion energies and ^{56}Ni masses. Moreover, up to $\sim 7 \times 10^{12}$ cm the ^{56}Ni mass tends to decrease with increasing radius, reaching a minimum for SN 2009E, and then rises again for

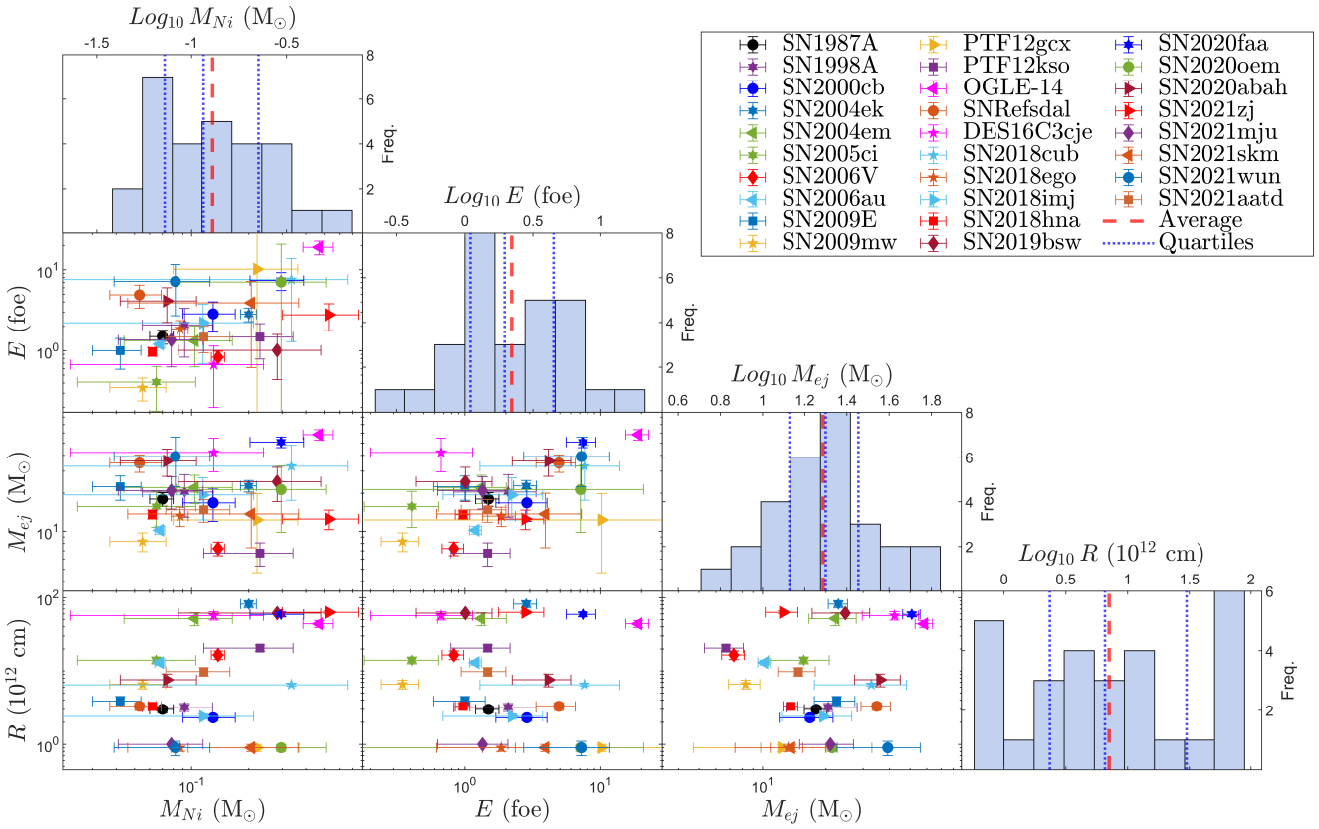

Fig. 5. Distribution of SNe physical properties. The diagonal panels show the histograms of the logarithm of each parameter ($M_{\rm Ni}$, E, $M_{\rm ej}$, R), with the mean value (dashed line) and quartiles (25%, 50%, and 75%; see dotted lines) indicated. The lower triangular panels show scatter plots of the parameter pairs for each SN in the sample.

the most extended progenitors. This trend is consistent with the intrinsic nature of 1987A-like SN LC, where the slow rise of the second peak depends sensitively on the initial radius and on the ^{56}Ni yield. This behavior further distinguishes the group with lower radii and energy from the more energetic and extended one, which would otherwise resemble standard SNe II were it not for their unusually high ^{56}Ni content (average ^{56}Ni mass for SN II population is $\sim$0.037 $\pm$ 0.005 $M_\odot$; Rodríguez et al. 2021).

The extended parameter space inferred from our modeling also enables a qualitative comparison with recent stellar-evolution predictions for BSG progenitors. In particular, the inferred explosion energies and ^{56}Ni masses follow the exponential trend expected from neutrino-driven explosion models (e.g., Schneider et al. 2025), while the broad range of ejecta masses and progenitor radii overlaps with those predicted by recent grids of pre-SN supergiant models (Schneider et al. 2024). However, most single-star models at solar metallicity struggle to produce sufficiently compact and massive blue supergiants, confirming that either lower metallicity evolution (e.g., Woosley 1988) or binary interaction and merger channels (e.g., Tsuna et al. 2025) may be required to explain the 1987A-like SNe. Moreover, the most energetic and ^{56}Ni-rich events in our sample may also invite comparison with pair-instability progenitor models (e.g., Terreran et al. 2017), which naturally predict large explosion energies and nickel yields (e.g., Kasen et al. 2011; Dessart et al. 2012).

Finally, note that the explosion parameters derived by SUPERBAM are consistent with those obtained in other previous works (see Table 3 of Paper I, and references therein), confirming the reliability of our approach (see also Sect. 2.2). In Sect. 4.2, a detailed analysis of correlations among these physical parameters, as well as between the physical and spectrophotometric properties of the sample, is presented.

4.2. Correlations

To investigate possible statistical links between the explosion properties and the spectrophotometric features of the 1987A-like SN sample, we computed the Spearman correlation coefficient (ρ_c) and evaluated its significance with a t-test for each parameter combination (see Fig. 6). As already discussed in Sect. 3.1, the ^{56}Ni mass correlates positively ($\rho_c > 0$) with the peak luminosity $L_{\rm M}$, with very high significance ($p \ll 0.01$). $M_{\rm Ni}$ also shows a positive correlation with the explosion energy ($p = 0.01$), in agreement with theoretical expectations that link larger nickel yields to more energetic explosions (e.g., Schneider et al. 2025). From the spectroscopic side, $M_{\rm Ni}$ appears correlated with the Fe II line, both in velocity ($p = 0.02$) and in pEW ($p = 0.02$). Interestingly, higher nickel masses are associated with weaker Fe II absorption but faster line velocities. A possible interpretation is that larger amounts of ^{56}Ni keep the recombination front and the photosphere at larger radii in the ejecta (see, e.g., Paper II), so that Fe II lines form in faster-moving layers where the Fe abundance is intrinsically lower. This effect would explain the counter-intuitive result that Ni-rich explosions show weaker Fe II features, not because of a reduced Fe content, but because the absorption originates in more external and less Fe-rich regions. Such behavior suggests that scaling relations for line velocities may need to explicitly account for

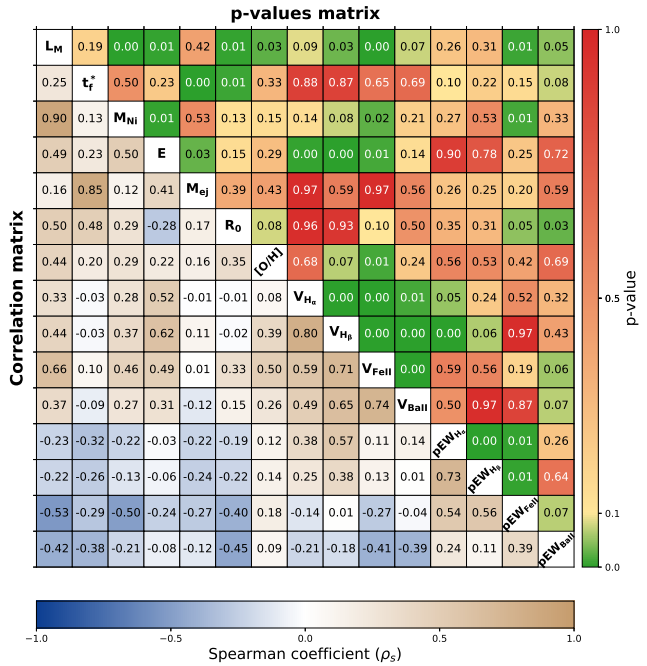

Fig. 6. Spearman correlation matrix for the physical and spectroscopic parameters considered. The lower-left half of squares show the Spearman correlation coefficient (ρ_c), color-coded from –1 (dark blue) to +1 (light brown), with the numerical values reported inside each cell. The upper-right half of squares show the associated p-values, color-coded according to significance level (from green for high significance to red for non–significant values). The diagonal reports the labels of the parameters. In addition to the parameters discussed in the previous sections, we also include [O/H] = 12+log(O/H) listed in Table 2.

the nickel mass. By contrast, the ejecta mass is strongly correlated with the recombination timescale t_f^*, as expected (Paper II), and shows a moderately significant trend with explosion energy ($p = 0.03$), but no direct correlation with ^{56}Ni mass. Spectroscopically, M_{ej} does not display connections with line properties.

As anticipated in Sect. 3.2, line velocities are mutually correlated, as are velocity widths, with the exception of Ba II, which does not follow the same trends. In fact, Ba II shows a particularly peculiar behavior. An anti-correlation emerges between its velocity and pEW, which becomes statistically significant ($p < 0.05$) once clear outliers (e.g., DES16C3cje) are excluded. This trend is consistent with the idea that more compact explosions, with less extended ejecta, retain higher densities in the line-forming regions and therefore favor stronger Ba II absorption (e.g., Mazzali & Chugai 1995). In support of this interpretation, the modeling results indicate an additional correlation with the progenitor radius at explosion, which appears to be inversely related to the Ba II's pEW. On the other hand, no correlation was found with other explosive parameters such as E and M_{Ni}. This suggests that the key factor regulating the intensity of the Ba II lines should be the compactness of the progenitors and ejecta, rather than differences in their nucleosynthetic production.

Progenitor radius also exhibits weak correlations with other parameters. In particular, an expected correlation between R_0 and the oxygen abundance [O/H] of the host environment is present in our analysis (e.g., Taddia et al. 2013, 2016). Curiously, metallicity itself shows possible links with both peak luminosity and expansion velocity. SNe in more metal-rich environments tend to expand faster and peak at higher luminosities. Although the significance is low, these trend could provide insights into the role of metallicity in shaping the properties of 1987A-like events.

However we note that correlation does not imply causation. Moreover, although the present sample is significantly larger than in previous works, it could not constitute a fully unbiased representation of the 1987A-like population. Selection effects linked to discovery methods, survey strategies, and spectroscopic follow-up may introduce statistical biases that affect both distributions and correlations. These results should therefore be used with caution, although they will gain robustness as the number of well-observed 1987A-like SNe increases in the coming years.

5. Summary and further consideration

In this work we introduced the novel procedure SuperBAM (Supernova Bayesian Analytic Modeling), a fast-modeling framework designed to infer the main physical properties of H-rich SNe from their bolometric LCs and spectroscopic information during the recombination phase. SuperBAM relies on Bayesian statistics and analytical prescriptions, providing posterior distributions for explosion energy, ejecta mass, progenitor radius, and synthesized ^{56}Ni mass. The method was validated against well-studied benchmarks and shown to reproduce the results of detailed numerical hydrodynamic simulations at a fraction of their computational cost.

We then applied SuperBAM to the most comprehensive sample of 87A-like SNe assembled so far (28 events), reconstructing their bolometric LCs in a homogeneous way and measuring spectroscopic features at maximum. The analysis reveals a heterogeneous population that nevertheless clusters into two broad groups: (i) lower-energy explosions with modest ^{56}Ni yields, reminiscent of SN 1987A, and (ii) more energetic events (sometimes exceeding 5 foe) with higher nickel production and, in some cases, unusually large progenitor radii. The parameter space, however, appears continuous, suggesting a spectrum of possible progenitor/explosion configurations rather than discrete categories.

From the statistical comparison of physical properties and spectrophotometric observables, we confirm the robust correlation between ^{56}Ni mass and both peak luminosity and explosion energy, as well as the strong link between ejecta mass and recombination timescale. We also identify a peculiar behavior of Ba II, whose line strength anti-correlates with velocity and appears inversely related to progenitor radius. This suggests that the prominent Ba absorption observed in many 87A-like events arises primarily from progenitor compactness and ejecta density, rather than from enhanced nucleosynthetic production. Notably, for progenitors with radii approaching $\sim 10^{13}$ cm, the Ba II strength converges toward that of standard SNe II ($\mathrm{pEW_{Ba\,II}} \sim 5$ Å; cf. Gutiérrez et al. 2017), supporting the interpretation that compactness, and not abundance anomalies, could be the key driver. Future progress on this front will require detailed spectral synthesis calculations that account for the thermodynamical state of the ejecta (temperature and density), in order to disentangle abundance from excitation effects.

Finally, several events display luminosity components not fully reproduced by standard recombination plus ^{56}Ni heating. The brightest SNe in our sample (e.g., OGLE-14 and SN 2020faa) require additional power sources such as magnetar spin-down or accretion, while others show early-time excesses consistent with interaction with CSM (e.g., SN 2021zj and SN 2021aatd). This highlights the need to extend fast-modeling frameworks similar to SuperBAM to incorporate

non-radioactive energy sources and CSM interaction, in order to capture the full diversity of 87A-like explosions. In particular, the inclusion of CSM-related components would allow us to constrain not only the explosion parameters but also the physical properties of the surrounding material. Combined with detailed spectroscopic analysis, this approach would provide key insights into the progenitor mass-loss history and the pre-explosion evolution leading to events such as SN 2021zj. A dedicated study of this object, including unpublished spectroscopic observations, is planned for future work.

The development of such efficient, Bayesian-based procedures is particularly timely in view of ongoing and upcoming large surveys (e.g., ZTF and LSST), which will discover thousands of peculiar SNe. SuperBAM represents a step toward scalable analysis pipelines, able to rapidly characterize large samples with improved accuracy over simple scaling relations and at a fraction of the cost of full numerical simulations. Moreover, our framework has proven effective even in the absence of spectroscopic information, providing physically meaningful estimates based solely on photometric data. This feature is particularly valuable for next-generation surveys, which will deliver extensive multi-band photometry but limited spectroscopic coverage. In this way, this work opens the path for systematic population studies of rare transients, bridging the gap between survey data and detailed physical modeling.

Acknowledgements. We acknowledge support from the Piano di Ricerca di Ateneo UNICT – Linea 2 PIA.CE.RI. 2024–2026 of Catania University (project AstroCosmo, P.I. A. Lanzafame). CI gratefully acknowledges the support received from the MERAC Foundation. SPC thanks Cardiff University for hosting him during the research activities that contributed to this work.

References

Arnett, W. D. 1980, ApJ, 237, 541
Arnett, D. 1996, Supernovae and Nucleosynthesis: An Investigation of the History of Matter from the Big Bang to the Present (Princeton University Press)
Arnett, W. D., Bahcall, J. N., Kirshner, R. P., & Woosley, S. E. 1989, ARA&A, 27, 629
Ashour, S. K., & Abdel-hameed, M. A. 2010, J. Adv. Res., 1, 341
Bellm, E. C., Kulkarni, S. R., Graham, M. J., et al. 2018, PASP, 131, 018002
Bersten, M. C., Benvenuto, O., & Hamuy, M. 2011, ApJ, 729, 61
Bianco, F. B., Ivezić, Ž., Jones, R. L., et al. 2021, ApJS, 258, 1
Bufano, F., Immler, S., Turatto, M., et al. 2009, ApJ, 700, 1456
Burrows, A. 1990, Ann. Rev. Nucl. Part. Sci., 40, 181
Cardelli, J. A., Clayton, G. C., & Mathis, J. S. 1989, ApJ, 345, 245
Catchpole, R., Menzies, J., Monk, A., et al. 1987, MNRAS, 229, 15P
Chatzopoulos, E., Wheeler, J. C., & Vinko, J. 2012, ApJ, 746, 121
Colgan, S. W. J., Haas, M. R., Erickson, E. F., Lord, S. D., & Hollenbach, D. J. 1994, ApJ, 427, 874
Cook, D. O., Kasliwal, M. M., Sistine, A. V., et al. 2019, ApJ, 880, 7
Cosentino, S. P. 2024, Ph.D. Thesis, Università degli Studi di Catania
Cosentino, S. P., Pumo, M. L., & Cherubini, S. 2025, MNRAS, 540, 2894
Dessart, L., Waldman, R., Livne, E., Hillier, D. J., & Blondin, S. 2012, MNRAS, 428, 3227
Dexter, J., & Kasen, D. 2013, ApJ, 772, 30
Fang, Q., Maeda, K., Ye, H., Moriya, T. J., & Matsumoto, T. 2024, ApJ, 978, 35
Gezari, S., Dessart, L., Basa, S., et al. 2008, ApJ, 683, L131
Graham, M. J., Kulkarni, S. R., Bellm, E. C., et al. 2019, PASP, 131, 078001
Grillo, C., Karman, W., Suyu, S. H., et al. 2016, ApJ, 822, 78
Gutiérrez, C. P., Anderson, J. P., Hamuy, M., et al. 2017, ApJ, 850, 90
Gutiérrez, C. P., Sullivan, M., Martinez, L., et al. 2020, MNRAS, 496, 95
Inserra, C., Smartt, S. J., Jerkstrand, A., et al. 2013, ApJ, 770, 128
Inserra, C., Prajs, S., Gutierrez, C. P., et al. 2018, ApJ, 854, 175
Jacobson-Galán, W. V., Dessart, L., Davis, K. W., et al. 2024, ApJ, 970, 189
Kasen, D., & Bildsten, L. 2010, ApJ, 717, 245
Kasen, D., & Woosley, S. E. 2009, ApJ, 703, 2205
Kasen, D., Woosley, S. E., & Heger, A. 2011, ApJ, 734, 102
Kelly, P. L., Brammer, G., Selsing, J., et al. 2016, ApJ, 831, 205
Khatami, D. K., & Kasen, D. N. 2019, ApJ, 878, 56
Khatami, D. K., & Kasen, D. N. 2024, ApJ, 972, 140
Kleiser, I. K. W., Poznanski, D., Kasen, D., et al. 2011, MNRAS, 415, 372
Lyman, J. D., Bersier, D., & James, P. A. 2014, MNRAS, 437, 3848
Martinez, L., & Bersten, M. C. 2019, A&A, 629, A124
Martinez, L., Anderson, J. P., Bersten, M. C., et al. 2022, A&A, 660, A42
Matsumoto, T., Metzger, B. D., & Goldberg, J. A. 2025, ApJ, 978, 56
Mazzali, P. A., & Chugai, N. N. 1995, A&A, 303, 118
Müller, T., Prieto, J. L., Pejcha, O., & Clocchiatti, A. 2017, ApJ, 841, 127
Nicholl, M. 2018, Res. Notes AAS, 2, 230
Nicholl, M., Guillochon, J., & Berger, E. 2017, ApJ, 850, 55
Orlando, S., Miceli, M., Pumo, M. L., & Bocchino, F. 2015, ApJ, 810, 168
Pastorello, A., Baron, E., Branch, D., et al. 2005, MNRAS, 360, 950
Pastorello, A., Pumo, M. L., Navasardyan, H., et al. 2012, A&A, 537, A141
Planck Collaboration VI. 2020, A&A, 641, A6
Popov, D. V. 1993, ApJ, 414, 712
Pumo, M. L., & Cosentino, S. P. 2025, MNRAS, 538, 223 (Paper II)
Pumo, M. L., & Zampieri, L. 2011, ApJ, 741, 41
Pumo, M. L., & Zampieri, L. 2013, MNRAS, 434, 3445
Pumo, M. L., Turatto, M., Botticella, M. T., et al. 2009, ApJ, 705, L138
Pumo, M. L., Cosentino, S. P., Pastorello, A., et al. 2023, MNRAS, 521, 4801 (Paper I)
Pun, C. S. J., Kirshner, R. P., Sonneborn, G., et al. 1995, ApJS, 99, 223
Roberts, S., Osborne, M., Ebden, M., et al. 2013, Phil. Trans. R. Soc. A: Math. Phys. Eng. Sci., 371, 20110550
Rodríguez, Ó., Meza, N., Pineda-García, J., & Ramirez, M. 2021, MNRAS, 505, 1742
Salmaso, I., Cappellaro, E., Tartaglia, L., et al. 2023, A&A, 673, A127
Schlafly, E. F., & Finkbeiner, D. P. 2011, ApJ, 737, 103
Schneider, F. R. N., Podsiadlowski, P., & Laplace, E. 2024, A&A, 686, A45
Schneider, F. R. N., Laplace, E., & Podsiadlowski, P. 2025, A&A, 700, A253
Silva-Farfán, J., Förster, F., Moriya, T. J., et al. 2024, ApJ, 969, 57
Singh, A., Sahu, D. K., Anupama, G. C., et al. 2019, ApJ, 882, L15
Sit, T., Kasliwal, M. M., Tzanidakis, A., et al. 2023, ApJ, 959, 142
Smartt, S. J. 2009, ARA&A, 47, 63
Smith, K. W., Fulton, M., Gillanders, J., et al. 2021, TNS AstroNote, 14, 1
Szalai, T., Könyves-Tóth, R., Nagy, A. P., et al. 2024, A&A, 690, A17
Taddia, F., Stritzinger, M. D., Sollerman, J., et al. 2012, A&A, 537, A140
Taddia, F., Sollerman, J., Razza, A., et al. 2013, A&A, 558, A143
Taddia, F., Sollerman, J., Fremling, C., et al. 2016, A&A, 588, A5
Takáts, K., Pignata, G., Bersten, M., et al. 2016, MNRAS, 460, 3447
Terreran, G., Pumo, M. L., Chen, T. W., et al. 2017, Nature, 1, 713
Tody, D. 1986, SPIE Conf. Ser., 627, 733
Tonry, J. L., Denneau, L., Heinze, A. N., et al. 2018, PASP, 130, 064505
Tsuna, D., Fuller, J., & Lu, W. 2025, arXiv e-prints [arXiv:2508.21116]
Turatto, M., Benetti, S., & Pastorello, A. 2007, AIP Conf. Ser., 937, 187
Utrobin, V. P., & Chugai, N. N. 2011, A&A, 532, A100
Utrobin, V. P., Wongwathanarat, A., Janka, H.-T., et al. 2021, ApJ, 914, 4
Villar, V. A., Guillochon, J., Berger, E., et al. 2017, ApJ, 851, L21
Woosley, S. E. 1988, ApJ, 330, 218
Woosley, S. E., Heger, A., & Weaver, T. A. 2002, Rev. Mod. Phys., 74, 1015
Xiang, D., Wang, X., Zhang, X., et al. 2023, MNRAS, 520, 2965
Yang, S., Sollerman, J., Chen, T. W., et al. 2021, A&A, 646, A22
Young, T. R. 2004, ApJ, 617, 1233
Zampieri, L., Pastorello, A., Turatto, M., et al. 2003, MNRAS, 338, 711

Appendix A: Probability distribution function

This appendix describes the procedure adopted to construct and transform the probability distributions used in SUPERBAM for both the prior and posterior inference. This process involves two main steps: (1) defining the PDFs associated with the measured spectrophotometric features, and (2) converting the distributions of both measured features and modeling parameters into PDFs for the SN physical properties through the scaling relations.

As described in Sect. 2.1.1, once the key observables $m_i = \{t_m, t_M, L_M, v_M, M_{Ni}\}$ are measured, each with corresponding upper (m_i^+) and lower (m_i^-) uncertainties, a continuous probability distribution must be assigned to each feature. To achieve this, SUPERBAM models each observable as a random variable following a skew-normal distribution (e.g., Ashour & Abdel-hameed 2010), which accounts for possible asymmetries in the measurement errors:

$$f_0(x) = \frac{2}{\omega\sqrt{2\pi}} \exp\left[-\frac{(x-\xi)^2}{2\omega^2}\right] \int_{-\infty}^{\alpha\left(\frac{x-\xi}{\omega}\right)} \frac{1}{\sqrt{2\pi}} e^{-\frac{t^2}{2}}\, dt.$$

The free parameters of the distribution (ω, ξ, and α) are determined so that the resulting mean, standard deviation, and skewness reproduce the measured central value and asymmetric uncertainties of each feature. In practice, we adopt the following punctual distribution assumptions based on the measured feature and its upper and lower uncertainties: the mode is set to $A = m_i$, the mean to $B = (2m_i + m_i^+ + m_i^-)/4$, and the standard deviation to $C = (m_i^+ - m_i^-)/2$. Under these assumptions, the shape parameter α is obtained by numerically solving the implicit relation (e.g., Ashour & Abdel-hameed 2010):

$$\frac{(4-\pi)\times\delta^3(\alpha)}{2[1-\delta^2(\alpha)]^{3/2}} + \text{sign}(\alpha)\,\frac{\exp[-2\pi/|\alpha|]}{1-\delta^2(\alpha)} = \frac{2(B-A)}{C},$$

where $\delta^2(\alpha) = 2\alpha^2/[\pi(1+\alpha^2)]$. Once α is known, the other PDF's parameters are computed as:

$$\omega = \frac{C}{\sqrt{1-\delta^2(\alpha)}}, \qquad \xi = B - \omega\,\delta(\alpha).$$

These relations ensure that the resulting skew-normal function accurately reproduces the observed asymmetry in the measurement uncertainties (see also Fig. 3.12 in Cosentino 2024).

Since all the measured features represent intrinsically positive quantities, their probability density must also be defined on a positive domain. However, the standard skew-normal distribution $f_0(x)$ is defined over the entire real line and thus allows non-physical (negative) values. To prevent this issue and ensure continuity at the origin, we introduce a corrective function that smoothly suppresses the probability below zero while preserving the original distribution shape for positive values:

$$f(x) = N \times f_0(x) \times \begin{cases} \exp\left[-\frac{x_0^2}{(x_0-\xi)^2}(x-\xi)^2/x^2\right] & x > 0 \\ 0 & x \le 0 \end{cases},$$

where x_0 is related to the lowest admitted value and N is a normalization constant. This correction maintains the position of the distribution maximum and reproduces the original skew-normal behavior for $x > x_0$.

As described in Sects. 2.1.1 and 2.1.3, the scaling relations provide a direct link between the observed features and the prior distributions of the physical parameters (E, M_{ej}, R_0), as well as between the model parameters (y_i, λ, k_1). Similarly, the posterior PDFs of the model parameters are related to the physical ones by applying the inverse transformations of the system described in Eq. 7.

In both cases, these transformations rely on the combination of independent random variables associated with the measured or inferred quantities. The operations between the involved PDFs can be reduced to two basic types:

- Power operations – Let $Y = X^\alpha$, with $k \in \mathbb{R}$ and $X > 0$ a random variable defined on a positive support with PDF $f(x)$. Then Y is also a positive random variable, whose PDF is given by
$$g(y) = \frac{1}{|k|}\, y^{(1-k)/k}\, f(y^{1/k}).$$
- Product operations – Let $Z = X\,Y$, where both $X > 0$ and $Y > 0$ are independent random variables with PDFs $f(x)$ and $g(y)$, respectively. Then Z is also defined on a positive support, with the following PDF:
$$h(z) = \int_0^{+\infty} f(x)\, g(z/x)\, \frac{1}{x}\, dx.$$

Since all variables involved in Eqs. 3 (or 4) and 10 are defined on a positive domain and independent, the combination of their PDFs can be performed using previous transformations.

Appendix B: Effects of ^{56}Ni mixing

In this appendix, we investigate the effects of varying the ^{56}Ni mixing parameter k_2, or equivalently the characteristic radius x_c, on the spatial distribution of radioactive material and on the resulting bolometric LC. This analysis is motivated by recent 3D simulations of SN 1987A (e.g., Utrobin et al. 2021), which predict significant outward mixing of ^{56}Ni.

Within our analytical framework, the ^{56}Ni distribution is described by an exponential profile characterized by the parameter x_c, defined such that 95% of the total nickel mass is enclosed within a comoving radius $x_c R_{ej}$ (see also Eqs. 27-29 of Paper II):

$$x_c = \sqrt[3]{\frac{\log\left[0.05 + 0.95 \times \exp\left(-k_2\right)\right]}{k_2}}. \tag{B.1}$$

The fiducial value adopted in this work, $k_2 = 32.87 \rightarrow x_c = 0.45$, is consistent with previous hydrodynamical models used for validation (Pumo & Zampieri 2011, 2013) and with classical prescriptions for nickel mixing (Young 2004).

Figure B.1 shows the mass fraction of ^{56}Ni as a function of ejecta shell velocity for the SN 1987A best-fit model, computed for different values of x_c and assuming comoving ejecta expansion. For the fiducial case ($x_c = 0.45$), less than 0.01% of the nickel mass reaches velocities above $\sim 2500\,\mathrm{km\,s^{-1}}$, slightly below the maximum velocities inferred from observations (e.g., Colgan et al. 1994) and from 3D simulations (Utrobin et al. 2021). This difference can be partly attributed to the simplified density structure assumed in the analytical model, which adopts a uniform ejecta density, unlike hydrodynamical models where the outer layers are less dense and expand at higher velocities (cf. Section 2.2). Increasing the mixing parameter to $x_c = 0.55$ results in a more extended nickel distribution with maximum velocities of around $3000\,\mathrm{km\,s^{-1}}$, comparable to those measured by Colgan et al. (1994).

Figure B.2 compares the bolometric LCs obtained for different values of x_c. A less confined nickel distribution leads to

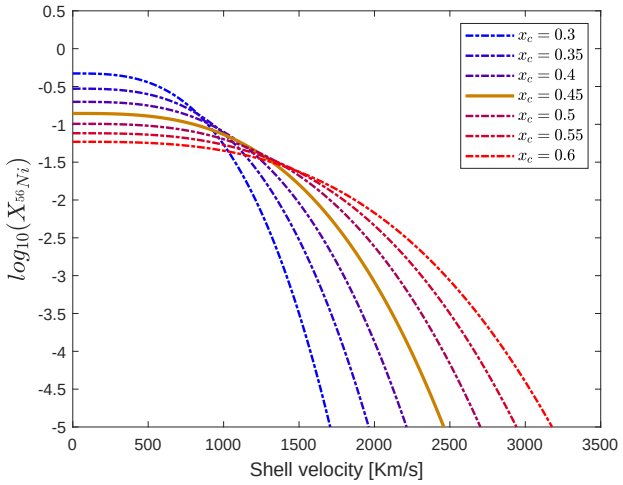

Fig. B.1. Abundance distribution of ^{56}Ni inside the ejecta shells as a function of shell velocity. Different curves refers to EXP-^{56}Ni distribution with different confinement coefficient x_c (Paper II).

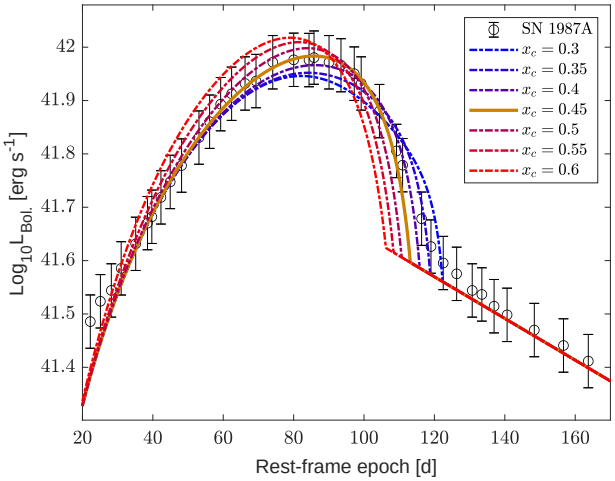

Fig. B.2. Effect of different ^{56}Ni mixing on the bolometric LC for SN 1987A.

a modest anticipation of the end of the recombination phase, with t_f shifting from $\sim$ 112 days (x_c = 0.45) to $\sim$ 108 days (x_c = 0.55), while remaining fully consistent within the observational uncertainties. In order to evaluate the effect of ^{56}Ni mixing on the physical parameters estimation, we further reapply the SUPERBAM fitting procedure using x_c = 0.55 (corresponding to k_2 = 18). The resulting best-fit parameters are very similar to those obtained for the fiducial case, with all parameters remaining unchanged within uncertainties, except for a modest increase in the ejecta mass from $\sim$ 17 M$_\odot$ to $\sim$ 19 M$_\odot$. This confirms that variations in the ^{56}Ni mixing parameter mainly induce second-order effects on the inferred physical properties, in agreement with what reported in Paper II and previous studies (e.g., Pumo & Zampieri 2013). We stress, however, that a more detailed photometric investigation of mixing effects critically relies on having accurate observations of the late recombination phase (immediately preceding the onset of the radioactive tail), where the impact of different mixing configurations becomes more pronounced.

Appendix C: Observational features and modeling

This appendix presents the main observational and modeling information for the 1987A-like SNe analysed in this work. Tab. C.1 summarizes the key photometric observables derived from the bolometric LCs, followed by Tab. C.2 reporting the spectral measurements (photospheric velocities and pseudo-equivalent widths) obtained from the published spectra (see also Tab. 2 and references therein). Tab. C.3 contains the physical parameters inferred through our SUPERBAM analysis.

Table C.1. Bolometric LC features of the 1987A-like SN sample.

SN Name	t_m	$\bar{t}_M$	L_M	t_f^*	M_{Ni}
SN1987A	$8.8^{+7.2}_{-5}$	$94^{+10.5}_{-13.8}$	85.95 ± 9.05	$112.6^{+5.9}_{-9.3}$	0.07 ± 0.01
SN1998A	$9.2^{+9.9}_{-9.2}$	$93.2^{+25.6}_{-30.2}$	104.48 ± 31.84	$118.9^{+0.1}_{-12.8}$	0.092 ± 0.037
SN2000cb	$7.8^{+3}_{-7.8}$	$88.5^{+16.4}_{-31}$	126.19 ± 44.78	$104.9^{+0.1}_{-8.2}$	0.13 ± 0.04
SN2004ek	$33.2^{+6.5}_{-13.2}$	$99.8^{+33.5}_{-20.5}$	459 ± 180.56	$158.9^{+24.9}_{-29.6}$	0.20 ± 0.02
SN2004em	39.8^{+0}_{-18}	$124.2^{+14.2}_{-27.8}$	246.85 ± 75.43	$140.9^{+32.6}_{-8.3}$	0.10 ± 0.06
SN2005ci	$19.3^{+1}_{-19.3}$	$110.2^{+10}_{-19.8}$	70.62 ± 9.06	$125.4^{+4.9}_{-7.6}$	0.065 ± 0.040
SN2006V	$22.8^{+1.9}_{-22.8}$	$83.2^{+11.5}_{-13.8}$	199.29 ± 24.31	$102.9^{+7.4}_{-9.8}$	0.138 ± 0.011
SN2006au	$20.5^{+15.8}_{-20.5}$	$75.2^{+9.5}_{-5.2}$	153.01 ± 7.87	$99.6^{+2.9}_{-12.2}$	0.068 ± 0.004
SN2009E	$10^{+0.1}_{-10}$	$106.5^{+17}_{-24.5}$	57.29 ± 12.57	$126.9^{+10.4}_{-10.2}$	0.042 ± 0.012
SN2009mw	$13.6^{+0.8}_{-13.6}$	$95.2^{+14.2}_{-16}$	62.17 ± 8.82	$111.6^{+7.9}_{-8.2}$	0.055 ± 0.018
PTF12gcx	$5^{+0.4}_{-5}$	$66.2^{+29.6}_{-33.5}$	289.83 ± 217.16	$95.9^{+0.1}_{-14.8}$	0.221 ± 0.141
PTF12kso	$23.3^{+29.1}_{-23.3}$	$81^{+14}_{-32.2}$	291.16 ± 65.57	$97.4^{+1.9}_{-8.2}$	0.229 ± 0.113
OGLE-14	$20.8^{+19.6}_{-20.8}$	$119^{+13}_{-16.5}$	1253.38 ± 193.62	$164.1^{+39.6}_{-22.6}$	0.469 ± 0.083
SNRefsdal	$8.8^{+0.8}_{-8.8}$	$74^{+28}_{-23.5}$	95.77 ± 9.92	$130.4^{+0.9}_{-28.2}$	0.053 ± 0.016
DES16C3cje	$39.8^{+0}_{-39.8}$	$213^{+66.6}_{-76.2}$	197.94 ± 1825.21	$279.6^{+0.1}_{-33.3}$	0.131 ± 0.108
SN2018cub	$13^{+26.8}_{-13}$	$117.8^{+13.6}_{-47.2}$	305 ± 144.43	$131.4^{+0.1}_{-6.8}$	0.335 ± 0.325
SN2018ego	5^{+8}_{-5}	$76.2^{+8.2}_{-10.5}$	105.12 ± 9.59	$102.9^{+0.1}_{-13.3}$	0.087 ± 0.009
SN2018imj	$7.9^{+2}_{-7.9}$	$95.8^{+17.4}_{-20}$	124.16 ± 16.6	$113.1^{+0.9}_{-8.7}$	0.115 ± 0.097
SN2018hna	$12.8^{+5}_{-3.8}$	$91.2^{+7.2}_{-7.2}$	85.49 ± 5.83	$105.6^{+10.9}_{-7.2}$	0.062 ± 0.003
SN2019bsw	$39.8^{+0}_{-39.8}$	$111.8^{+4.6}_{-30.5}$	218.84 ± 64.5	$116.4^{+0.1}_{-2.3}$	0.282 ± 0.197
SN2020faa	$39.8^{+0}_{-39.8}$	$147^{+27.5}_{-26.2}$	779.46 ± 144.71	$193.9^{+8.4}_{-23.4}$	0.296 ± 0.093
SN2020oem	$5^{+3.6}_{-5}$	$93.5^{+23.9}_{-39.2}$	269.52 ± 105.37	$117.4^{+0.1}_{-11.9}$	0.296 ± 0.213
SN2020abah	$13.8^{+26}_{-13.8}$	$103^{+30.8}_{-26.8}$	132.61 ± 42.7	$141.9^{+17.6}_{-19.4}$	0.074 ± 0.032
SN2021zj	$39.8^{+0}_{-13.2}$	$112.2^{+14.8}_{-34.2}$	681.83 ± 206.42	$128.6^{+0.1}_{-8.2}$	0.526 ± 0.225
SN2021mju	$5^{+3.2}_{-5}$	$98^{+8.9}_{-19.8}$	52.34 ± 22.69	$106.9^{+0.1}_{-4.4}$	0.078 ± 0.037
SN2021skm	$5^{+0.3}_{-5}$	$84.8^{+14.1}_{-29.2}$	162.48 ± 48.75	$98.9^{+0.1}_{-7.1}$	0.21 ± 0.16
SN2021wun	$5^{+0.4}_{-5}$	$91.2^{+46.4}_{-30.8}$	95.72 ± 39.3	$137.6^{+0.1}_{-23.2}$	0.082 ± 0.043
SN2021aatd	$16.3^{+21.7}_{-16.3}$	$92.5^{+13}_{-13.8}$	160.35 ± 21.01	$113.1^{+3.9}_{-10.3}$	0.116 ± 0.043

Notes. Characteristic times (t_m, $\bar{t}_M$, t_f^*) are expressed in days. L_M is in units of 10^{41} erg s^{-1} and M_{Ni} in solar masses.

Table C.2. Main spectroscopic features of the 1987A-like SN sample.

SN name	Spectra date [MJD]	Rest-Frame Epoch [d]	V_{H_α} [km/s]	pEW$_{H_\alpha}$ [Å]	V_{H_β} [km/s]	pEW$_{H_\beta}$ [Å]	$V_{Fe\,II}$ [km/s]	pEW$_{Fe\,II}$ [Å]	$V_{Ba\,II}$ [km/s]	pEW$_{Ba\,II}$ [Å]
SN1987A	46934	84	5071 ± 50	57.5 ± 1.9	4019 ± 38	10.1 ± 0.9	2268 ± 53	23.9 ± 1.0	2372 ± 27	18.7 ± 6.0
SN1998A	50894	92	7519 ± 169	72.0 ± 0.8	5830 ± 172	63.0 ± 2.6	3643 ± 22	26.6 ± 0.5	2979 ± 75	6.8 ± 1.0
SN2000cb	51722	71	8879 ± 56	106.1 ± 2.7	7479 ± 48	51.2 ± 1.4	4269 ± 22	20.5 ± 1.0	3675 ± 7	11.8 ± 1.0
SN2004ek	53328	76	5994 ± 33	3.1 ± 0.1	5838 ± 45	11.5 ± 0.5	4798 ± 47	9.2 ± 0.5	4959 ± 35	1.3 ± 0.0
SN2004em	53328	64	7715 ± 271	84.7 ± 8.3	6448 ± 68	30.3 ± 2.4	4895 ± 25	20.2 ± 1.4	5015 ± 225	6.0 ± 1.0
SN2005ci	53621	108	6378 ± 65	82.1 ± 1.7	5421 ± 84	47.7 ± 1.3	2639 ± 59	17.7 ± 1.3	1443 ± 34	12.3 ± 2.0
SN2006V	53822	73	5886 ± 238	38.7 ± 3.8	3721 ± 301	20.7 ± 4.5	2961 ± 9	23.2 ± 0.8	3842 ± 151	7.8 ± 1.0
SN2006au	53850	56	7434 ± 180	59.3 ± 1.8	5958 ± 178	39.9 ± 1.4	4519 ± 16	20.6 ± 1.4	3820 ± 115	6.3 ± 1.0
SN2009E	54922	97	5572 ± 187	20.0 ± 2.1	1706 ± 185	2.8 ± 0.4	1570 ± 26	15.6 ± 0.6	2230 ± 6	21.0 ± 1.0
SN2009mw	55267	91	7296 ± 163	87.8 ± 2.0	5792 ± 164	50.5 ± 1.3	3015 ± 23	29.2 ± 0.7	2496 ± 6	3.8 ± 0.0
PTF12gcx	56134	50	7715 ± 306	84.7 ± 8.3	7795 ± 156	23.3 ± 1.1	4446 ± 104	16.9 ± 2.2	4776 ± 85	8.4 ± 1.0
PTF12kso	56238	61	9369 ± 119	108.7 ± 1.7	6801 ± 117	47.4 ± 1.2	3822 ± 59	11.6 ± 0.8	4139 ± 159	2.8 ± 2.0
OGLE-14	56974	101	8849 ± 331	47.2 ± 2.8	7119 ± 326	29.4 ± 1.3	4917 ± 48	8.7 ± 0.9	–	–
SN Refsdal	57021	21	8400 ± 500[a]	–	–	–	–	–	–	–
DES16C3cje	57805	127	1359 ± 31	7.1 ± 0.1	1088 ± 51	7.6 ± 0.2	1370 ± 19	10.3 ± 0.0	875 ± 19	2.4 ± 0.0
SN2018cub	58335	114	8399 ± 36	55.7 ± 4.6	6456 ± 216	39.5 ± 1.6	3587 ± 249	19.3 ± 0.5	3426 ± 110	6.0 ± 3.0
SN2018ego	58373	120	7989 ± 242	58.3 ± 8.5	6179 ± 244	45.7 ± 7.0	4238 ± 147	17.1 ± 0.6	–	–
SN2018imj	58487	106	6825 ± 189	86.0 ± 2.9	5510 ± 59	49.7 ± 2.4	2977 ± 405	31.3 ± 11.4	2081 ± 104	17.1 ± 1.0
SN2018hna	58483	72	6948 ± 142	21.2 ± 1.7	4047 ± 1006	13.4 ± 11.8	3456 ± 22	16.3 ± 1.0	3354 ± 171	1.4 ± 1.0
SN2019bsw	58562	77	7306 ± 171	79.1 ± 1.7	6060 ± 122	30.4 ± 3.4	3305 ± 91	16.7 ± 6.0	3332 ± 80	13.7 ± 2.0
SN2020faa	59076	144	7546 ± 509	42.7 ± 5.8	5933 ± 37	18.8 ± 1.3	4591 ± 74	10.9 ± 0.7	3077 ± 76	1.0 ± 0.0
SN2020oem	59090	103	5656 ± 201	40.1 ± 3.7	–	–	–	–	–	–
SN2020abah	59195	19	9475 ± 141	116.1 ± 9.8	8088 ± 14	22.8 ± 1.8	4051 ± 273	18.2 ± 3.3	4399 ± 420	5.6 ± 2.0
SN2021mju	59365	75	7048 ± 83	76.9 ± 1.4	–	–	–	–	5483 ± 1336	–
SN2021skm	59438	47	7911 ± 199	31.0 ± 4.7	5236 ± 54	7.0 ± 0.3	3132 ± 82	8.9 ± 3.3	2284 ± 155	9.9 ± 2.0
SN2021wun	59468	42	7642 ± 438	50.2 ± 1.5	–	–	2243 ± 331	19.0 ± 6.6	3619 ± 25	4.3 ± 1.0
SN2021aatd	59592	98	6099 ± 94	65.9 ± 11.8	5108 ± 231	48.8 ± 6.9	3691 ± 56	15.4 ± 3.4	2454 ± 534	7.0 ± 5.5

Notes. In the second and third columns, the spectra acquisition time in MJD and the SN rest-frame epoch (since the explosion) are reported, respectively. [(a)] The spectrum of SN Refsdal is not optical and its V_{H_α} value is taken from Kelly et al. (2016).

Table C.3. Physical parameters of the 1987A-like SN sample derived by SUPERBAM procedure.

SN Name	Energy [foe]			Ejected Mass [$M_\odot$]			Initial Radius [10^{12} cm]		
	Pr.	Po.	MC	Pr.	Po.	MC	Pr.	Po.	MC
SN1987A	1.4 ± 0.9	1.5 ± 0.2	1.4 ± 0.3	16 ± 5	18 ± 1	17 ± 2	4.4 ± 3.6	3. ± 0.2	3 ± 0.3
SN1998A	4.1 ± 3.8	2.08 ± 0.87	2.28 ± 1.25	24 ± 14.2	20.5 ± 3.2	21.3 ± 7.6	4.8 ± 4.6	3.2 ± 0.3	3.2 ± 0.4
SN2000cb	6.12 ± 6.01	2.85 ± 0.88	2.4 ± 1.16	24.7 ± 14.3	16.8 ± 1.9	14.7 ± 4.8	3.3 ± 2.6	2.3 ± 0.2	2.3 ± 0.2
SN2004ek	11.63 ± 8.98	2.82 ± 0.31	2.83 ± 0.54	37.3 ± 19.4	22.9 ± 1	22.9 ± 2.4	44.1 ± 23.2	81.7 ± 4.1	82.3 ± 9.4
SN2004em	20.41 ± 13.65	1.32 ± 0.57	1.38 ± 0.69	50.7 ± 18.4	22.2 ± 3.6	23.9 ± 5.6	53.1 ± 22.3	51.7 ± 4.4	54.7 ± 10.4
SN2005ci	4.66 ± 2.42	0.41 ± 0.19	0.44 ± 0.23	27.8 ± 8	15.7 ± 2.8	16.3 ± 5	15.1 ± 10.3	14 ± 1.3	13.9 ± 1.5
SN2006au	9.58 ± 6.32	1.2 ± 0.08	1.2 ± 0.12	24.4 ± 7	10.2 ± 0.3	10.2 ± 0.7	24.5 ± 21.2	13 ± 0.7	13.2 ± 1
SN2006V	2.19 ± 1.28	0.83 ± 0.08	0.86 ± 0.15	16.6 ± 5.3	7.3 ± 0.3	7.5 ± 0.9	21.9 ± 15.3	16.5 ± 1.5	16.7 ± 2.2
SN2009E	0.81 ± 0.5	1 ± 0.32	1.03 ± 0.41	15.2 ± 5.8	22.5 ± 2.6	22.4 ± 4.9	3.9 ± 2.6	3.9 ± 0.6	4 ± 0.6
SN2009mw	3.66 ± 2.79	0.35 ± 0.09	0.35 ± 0.11	22.2 ± 8.5	8.3 ± 0.7	8.3 ± 1.4	7.6 ± 5.2	6.6 ± 0.6	6.5 ± 0.9
PTF12gcx	4.49 ± 4.29	10.21 ± 7.85	13.06 ± 94.15	20.1 ± 14.5	12.3 ± 4.1	11.5 ± 7.6	1 ± 0.7	0.9 ± 0.1	0.9 ± 0.1
PTF12kso	3.12 ± 3.35	1.47 ± 0.57	1.58 ± 0.68	18.2 ± 11.6	6.7 ± 0.9	6.9 ± 1.4	29.9 ± 29.4	20.5 ± 1.9	20.5 ± 2.1
OGLE14-73	19.1 ± 8.85	19 ± 3.16	18.91 ± 3.68	48.9 ± 12.8	58.3 ± 3.3	58 ± 5.5	24.9 ± 22.6	43.9 ± 2.2	44 ± 4.8
SNRefsdal	9.35 ± 8.67	4.9 ± 1.24	5.1 ± 1.57	26.8 ± 17.2	34.8 ± 3.2	35.5 ± 5.5	3.3 ± 2.3	3.3 ± 0.3	3.3 ± 0.4
DES16C3cje	4.12 ± 3.9	0.67 ± 0.41	0.74 ± 0.47	56.7 ± 35.7	42.2 ± 10.6	45.2 ± 12.5	60.5 ± 40	56.9 ± 6.7	54.3 ± 7.4
SN2018ego	5.76 ± 2.54	1.85 ± 0.22	1.89 ± 0.5	21 ± 5.4	13.2 ± 0.6	13.2 ± 2.3	1.3 ± 1.4	0.9 ± 0.1	0.9 ± 0.1
SN2018hna	4.14 ± 2.78	0.97 ± 0.05	0.99 ± 0.12	21.9 ± 6	13.6 ± 0.2	13.7 ± 1.1	7.6 ± 4.6	3.3 ± 0.2	3.3 ± 0.3
SN2018imj	4.3 ± 3.39	2.21 ± 1.35	2.16 ± 1.52	23.8 ± 10.3	19.4 ± 4.9	19 ± 7.1	3 ± 2.3	2.4 ± 0.2	2.3 ± 0.2
SN2018lrq	30.34 ± 29.05	2.81 ± 1	2.67 ± 1.22	52.1 ± 27	38.6 ± 4.9	36.8 ± 10.7	1.4 ± 1.3	0.9 ± 0.1	0.9 ± 0.1
SN2019bsw	7.1 ± 3.74	1.01 ± 0.53	0.98 ± 0.57	31.4 ± 10.1	24.7 ± 5.1	23.9 ± 7.5	60.5 ± 40	61.3 ± 1.2	61.3 ± 1.3
SN2020faa	39.16 ± 27.35	7.37 ± 1.75	7.35 ± 1.83	77 ± 30	50.9 ± 4.2	50.8 ± 4.8	60.5 ± 40	59.1 ± 2	59.4 ± 3.6
SN2020abah	8.95 ± 8.24	4.11 ± 1.41	4.38 ± 1.88	35 ± 20.2	36.1 ± 4.5	38.4 ± 8.8	9.2 ± 10.5	7.6 ± 0.9	8 ± 1.5
SN2020oem	3.71 ± 4.02	7.07 ± 5.28	7.06 ± 13.67	23.8 ± 16.3	21.4 ± 6.6	19.7 ± 11.6	1.5 ± 1.2	0.9 ± 0.1	0.9 ± 0.1
SN2021zj	24.36 ± 17.72[a]	2.78 ± 0.9	2.87 ± 1.02	53.7 ± 25.8[a]	12.5 ± 1.4	12.7 ± 2.2	54.1 ± 17.6	62.8 ± 2.2	62.4 ± 2.9
SN2021mju	24.7 ± 20.31	1.35 ± 0.63	1.36 ± 0.72	41.6 ± 16.3	21 ± 3.6	20.6 ± 6	1.5 ± 1.2	1.0 ± 0.1	1.0 ± 0.1
SN2021skm	3.2 ± 2.75	3.9 ± 2.8	3.76 ± 3.28	18.7 ± 9.6	13.7 ± 4	13.5 ± 6.3	1 ± 0.7	0.9 ± 0.1	0.9 ± 0.1
SN2021wun	1.3 ± 1.45	7.17 ± 3.2	7.41 ± 4.47	19 ± 14.3	39.2 ± 6.6	39.9 ± 16.6	1 ± 0.7	0.9 ± 0.1	0.9 ± 0.2
SN2021aatd	5.03 ± 4.36	1.47 ± 0.46	1.37 ± 0.53	23.8 ± 10	14.8 ± 1.7	14 ± 3	14.4 ± 14.4	9.8 ± 1.1	9.6 ± 1.3

Notes. The table is organized with the SN names in the first column, followed by nine columns clustered into triplets. Each triplet corresponds to a primary physical parameter–E, M_{ej}, and R_0–and contains three sub-columns reporting the values obtained via the different validation methods discussed in Sect. 2.2. [(a)] Different from other SNe in the sample, the E and M_{ej} prior estimates for SN 2021zj were obtained through the pure photometric scaling relations in Eq. 4 (see Sect. 2.1.1 for further details).